SANDIA REPORT

SAND2002-0340
Unlimited Release
Printed March 2002

Characterization of SF6 / Argon Plasmas for Microelectronics Applications

G. A. Hebner, I. G. Abraham, and J. R. Woodworth

Prepared by
Sandia National Laboratories
Albuquerque, New Mexico 87185 and Livermore, California 94550

Sandia is a multiprogram laboratory operated by Sandia Corporation, a Lockheed Martin Company, for the United States Department of Energy under Contract DE-AC04-94AL85000.

Issued by Sandia National Laboratories, operated for the United States Department of Energy by Sandia Corporation.

Available to DOE and DOE contractors from
U.S. Department of Energy
Office of Scientific and Technical Information
P.O. Box 62
Oak Ridge, TN 37831

Telephone: (865)576-8401
Facsimile: (865)576-5728
E-Mail: reports@adonis.osti.gov
Online ordering: http://www.doe.gov/bridge

Available to the public from
U.S. Department of Commerce
National Technical Information Service
5285 Port Royal Rd
Springfield, VA 22161

Telephone: (800)553-6847
Facsimile: (703)605-6900
E-Mail: orders@ntis.fedworld.gov
Online order: http://www.ntis.gov/ordering.htm

SAND2002-0340
Unlimited Release
Printed March 2002

Characterization of SF_6 / Argon plasmas for microelectronics applications

Gregory. A. Hebner, Ion. C. Abraham and Joseph. R. Woodworth
Plasma Sciences Department
Sandia National Laboratories
P.O. Box 5800
Albuquerque, NM 87185-1423

Abstract

This report documents measurements in inductively driven plasmas containing SF_6 / Argon gas mixtures. The data in this report is presented in a series of appendices with a minimum of interpretation. During the course of this work we investigated: the electron and negative ion density using microwave interferometry and laser photodetachment; the optical emission; plasma species using mass spectrometry, and the ion energy distributions at the surface of the rf biased electrode in several configurations. The goal of this work was to assemble a consistent set of data to understand the important chemical mechanisms in SF_6 based processing of materials and to validate models of the gas and surface processes.

Table of contents

Project Overview

The purpose of this report is to document measurements in inductively driven plasmas containing SF_6 / Argon gas mixtures. During the course of this work a number of measurements were performed to begin to assemble a consistent set of data to 1) understand the important physical and chemical mechanisms active in SF_6 based processing of microelectronic materials and 2) to generate a data set to validate models of the gas and surface processes, including feature evolution. While SF_6 has been used for many years in plasma processes, there is a significant lack of fundamental data of the type required to validate models.

Results from the various measurements are presented in a series of appendices. The appendices include a brief description of the measurement technique and then the data. In many cases, there is a minimum of interpretation. Appendix 1 includes the results of optical emission measurements of SF_6 gas mixtures over a range of powers and pressures. Appendix 2 reviews data obtained using a mass spectrometer. A mass spectrometer was used to survey the ion and neutral species present in the plasma and in the case of ion species, measure the scaling with plasma condition. Appendix 3 is a preprint of a paper submitted to the Journal of Applied Physics on measurements of the electron and negative ion density in SF_6 / Ar gas mixtures. Appendix 4 is a preprint of a paper submitted to the Journal of Vacuum Science and Technology A on measurements of the ion energy at the surface of a rf biased electrode with surface features.

Finally, we note that this work was the outgrowth of a funds-in CRADA with Motorola Corporation. We appreciate their support and access to their problems. The authors acknowledge the contributions of P. A. Miller, R. J. Shul, I. C. Abraham, B. P. Aragon, T. W. Hamilton and C. G. Willison to this work.

This work was performed at Sandia National Laboratories and supported by Motorola and Sandia National Laboratories. Sandia is a multiprogram laboratory operated by Sandia Corporation, a Lockheed Martin Company, for the United States Department of Energy under contract DE-AC04-94AL85000.

Appendix 1

Optical Emission Measurements In $Ar/SF_6/C_4F_8$ Discharges

Experimental Conditions

The experiments were performed in the GEC Reference Cell. The Cell had the anodized Al ICP window holder and the fused silica ring in place. Two wafer surfaces, silicon and oxide (fused silica) wafer were used.

Two mixtures of Ar/SF_6, 10/90 and 50/50, and pure C_4F_8 discharges were investigated. The 10/90 Ar/SF_6 mixture was investigated using actinometry (F atom line at 703.75 nm intensity ratio vs. Ar atom line at 750.39 nm). We could not sustain a pure SF_6 discharge with the oxide wafer in place. The center of the matrix of power and pressure conditions was at 10 mTorr total pressure, 10 sccm total flow rate, 200 W ICP coil power, and 20 W rf-bias power.

The light emitted from the plasma was dispersed using a Jobin HR460 monochromator with a 50 μm slit width, and a 300 lines/mm grating, and detected using a Princeton Instruments camera, set for 0.1 or 0.5 s exposure times, depending on the line intensities in the particular region. Six spectral regions, spanning from 190 nm to 850 nm, were calibrated using Ne, Ar, Kr, and Hg lamps.

The following 14 pages contains our optical emission data. In the trend plots *vs*. power, pressure, and rf-bias, the series marked "broad" is an integrated signal level for particular regions in the spectra with no detectable line features, just a broad emission envelope, which may be correlated with SiF_3 or CF_3 (in C_4F_8 plasmas). One region was integrated for Ar/SF_6 plasmas, from 340-380 nm, and three regions were integrated and added together for C_4F_8 plasmas, from 240-280 nm, from 340-355 nm, and from 640-660 nm. The wavelengths that were used for the other species identified in the trend plots were: SiF = 440 nm, SiF_2 = 390.15 nm, SF_x = 289.3 nm, Si = 576.3 nm. In order to show the trends for different species whose emission intensities could vary by orders of magnitude on the same graph, the intensities were scaled such that the highest intensity for a given emitting species in a given trend was assigned a value of 1.0, with the emission intensity of that species at the other conditions in the trend being proportionately smaller.

10/90 Ar/SF_6 10 mTorr 200 W ICP coil power 20 W rf-bias power silicon wafer

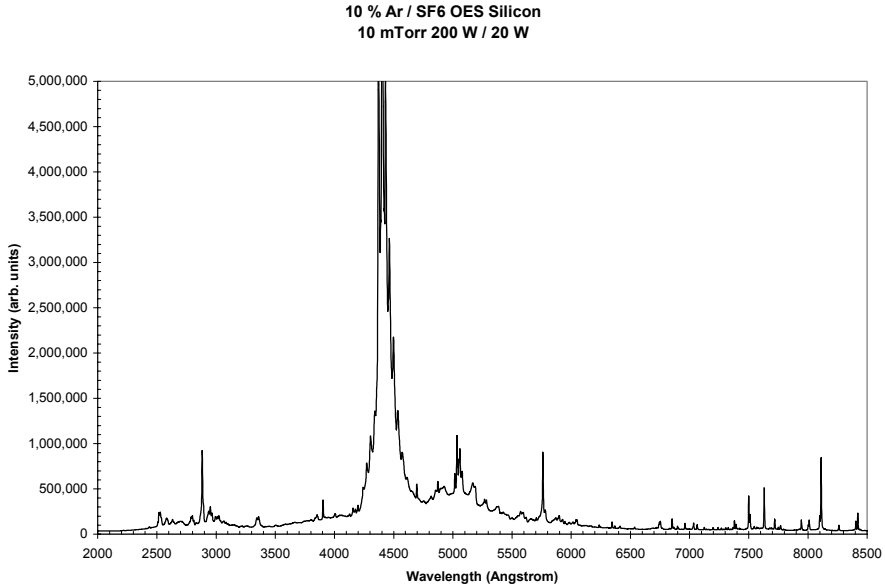

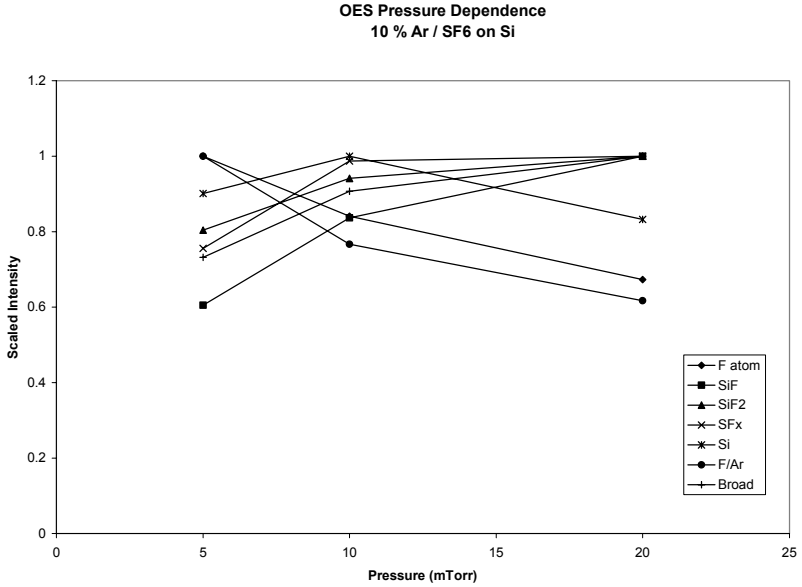

OES Inductive Power Dependence
10 % Ar / SF6 on Si

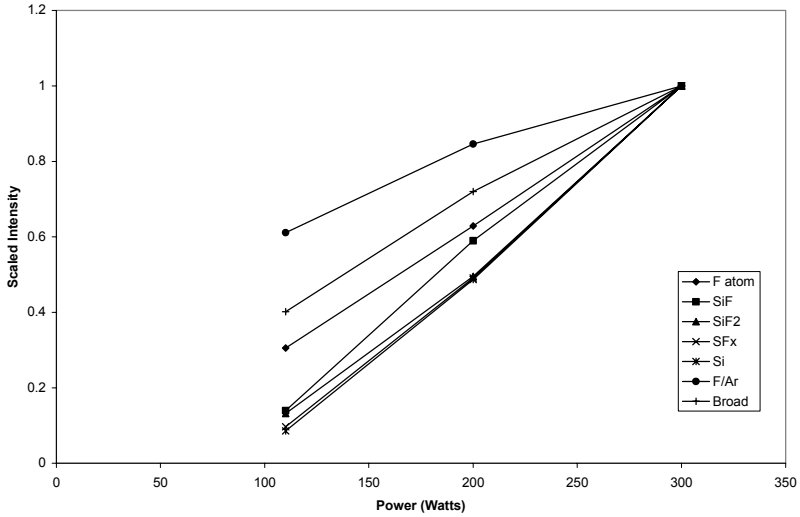

OES Bias Power Dependence
10 % Ar / SF6 on Si

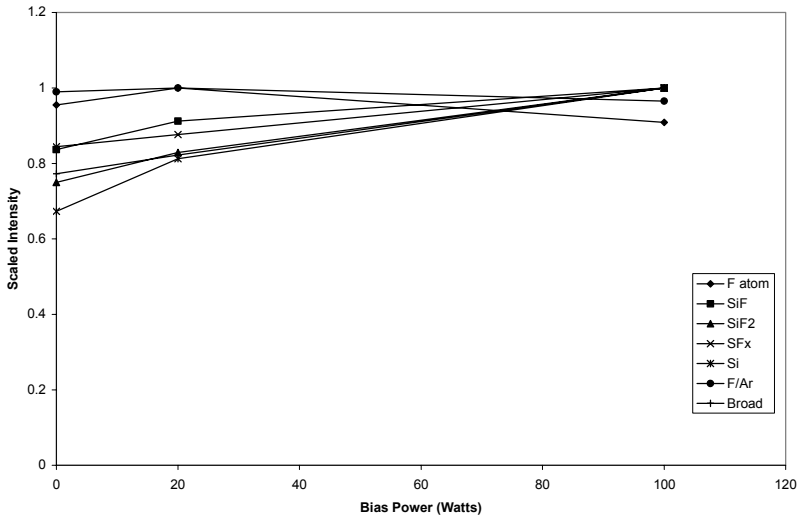

50/50 Ar/SF_6 10 mTorr 200 W ICP coil power 20 W rf-bias power silicon wafer

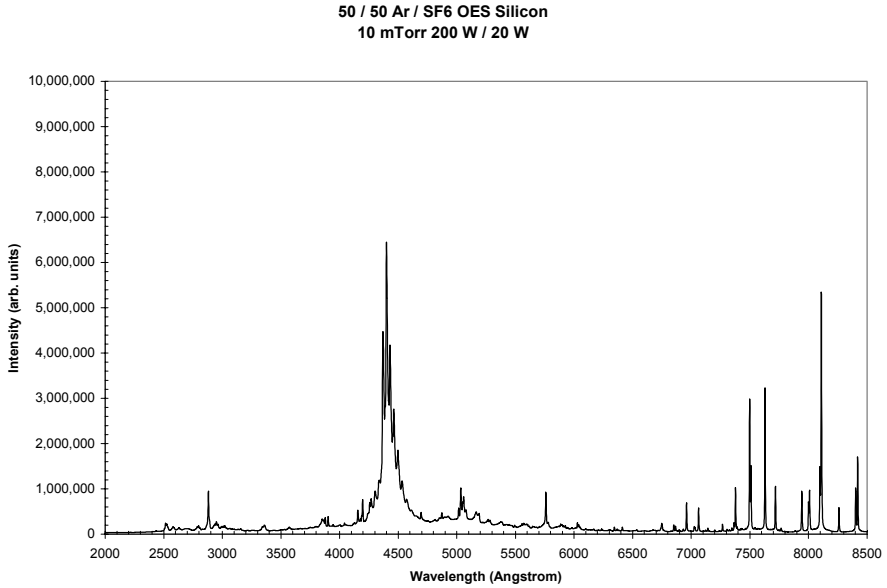

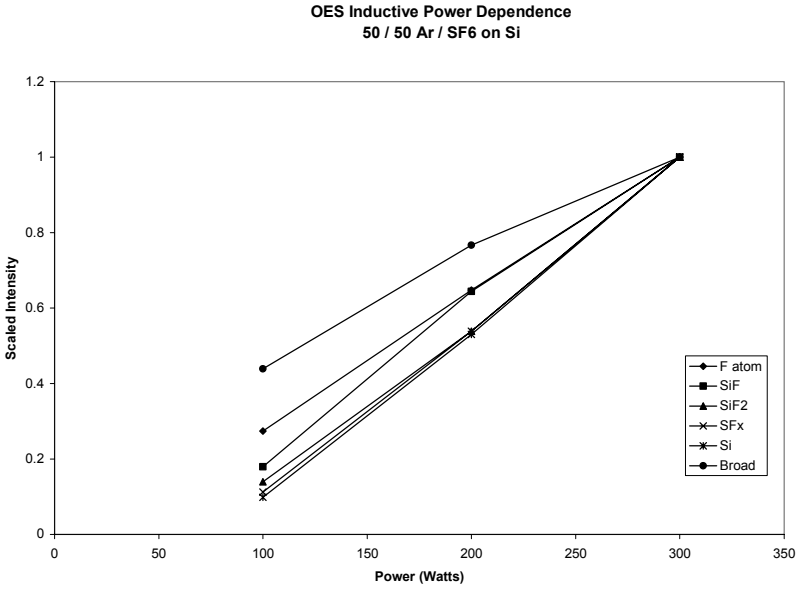

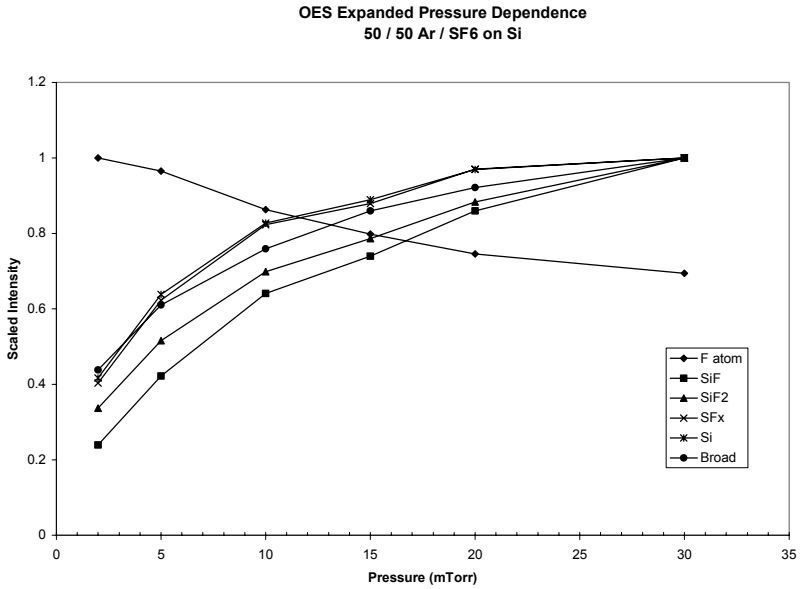
OES Expanded Pressure Dependence
50 / 50 Ar / SF6 on Si
Scaled Intensity
Pressure (mTorr)
F atom
SiF
SiF2
SFx
Si
Broad

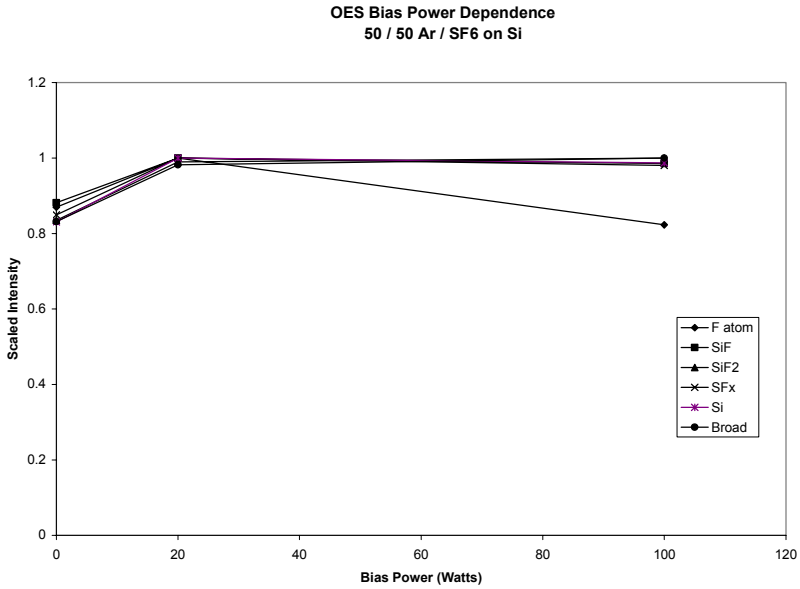
OES Bias Power Dependence
50 / 50 Ar / SF6 on Si
Scaled Intensity
Bias Power (Watts)
F atom
SiF
SiF2
SFx
Si
Broad

50/50 Ar/SF_6 10 mTorr 200 W ICP coil power 20 W rf-bias power quartz wafer

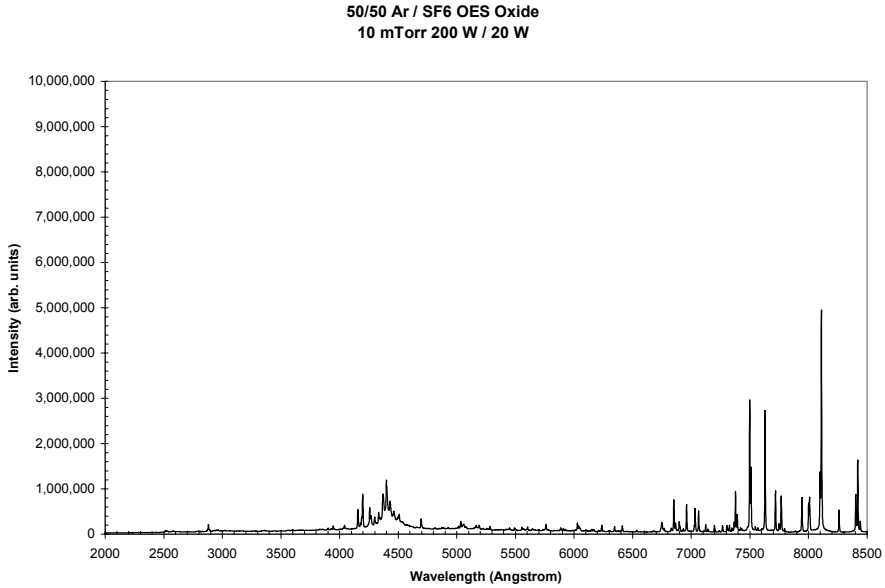

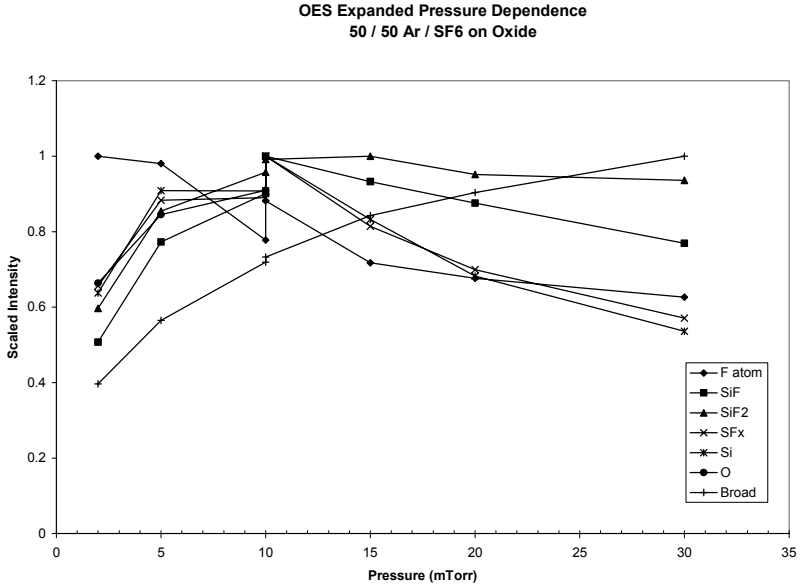

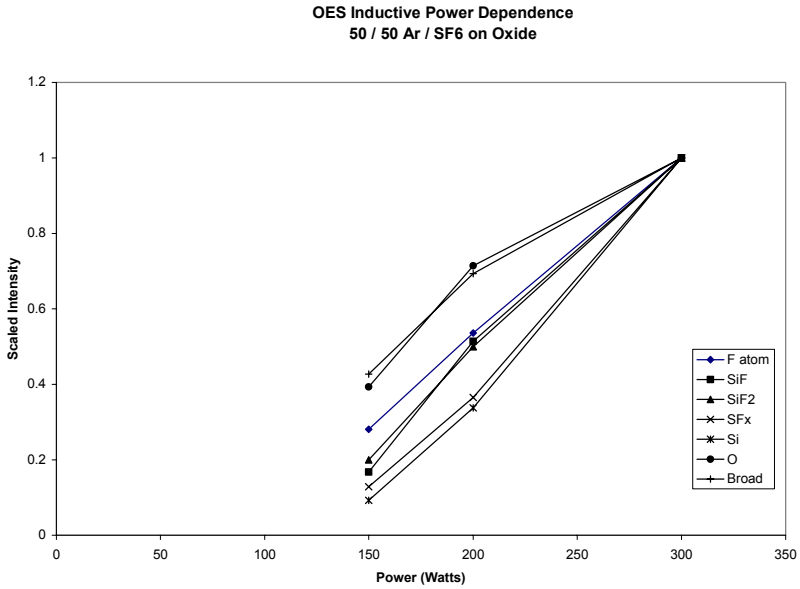
OES Inductive Power Dependence
50 / 50 Ar / SF6 on Oxide
Scaled Intensity
Power (Watts)
F atom
SiF
SiF2
SFx
Si
O
Broad

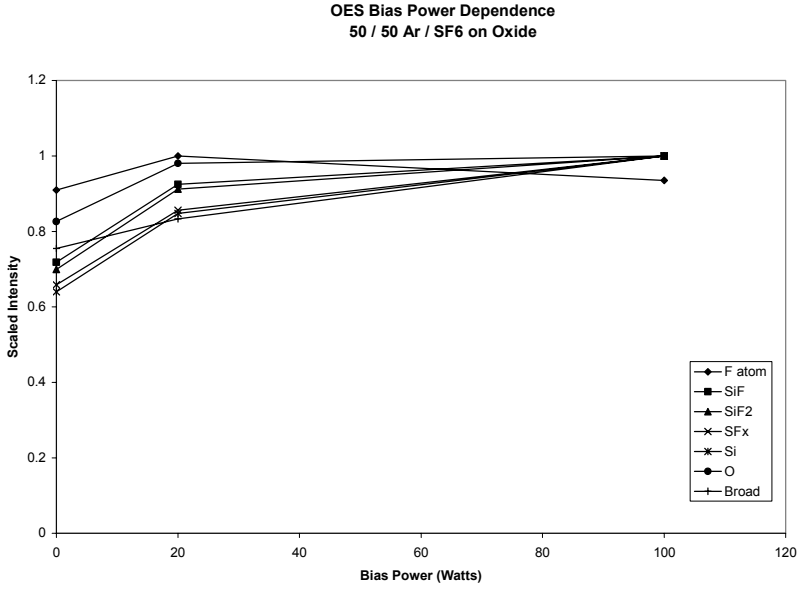
OES Bias Power Dependence
50 / 50 Ar / SF6 on Oxide
Scaled Intensity
Bias Power (Watts)
F atom
SiF
SiF2
SFx
Si
O
Broad

C_4F_8 Plasma 10 mTorr 200 W ICP coil power 20 W rf-bias power silicon wafer

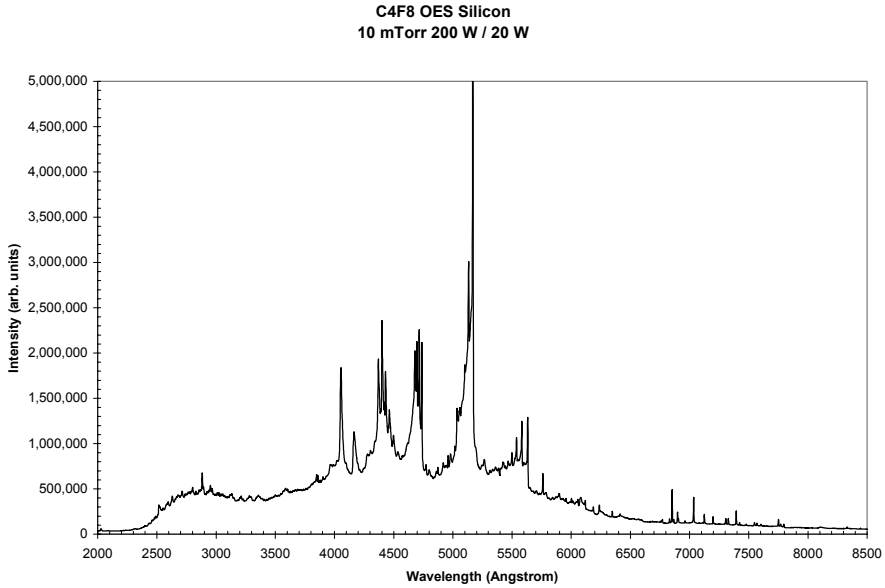

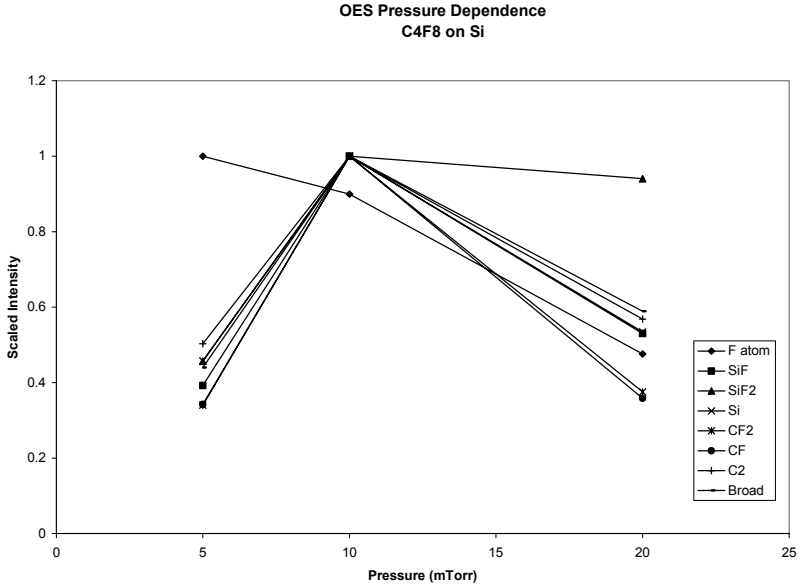

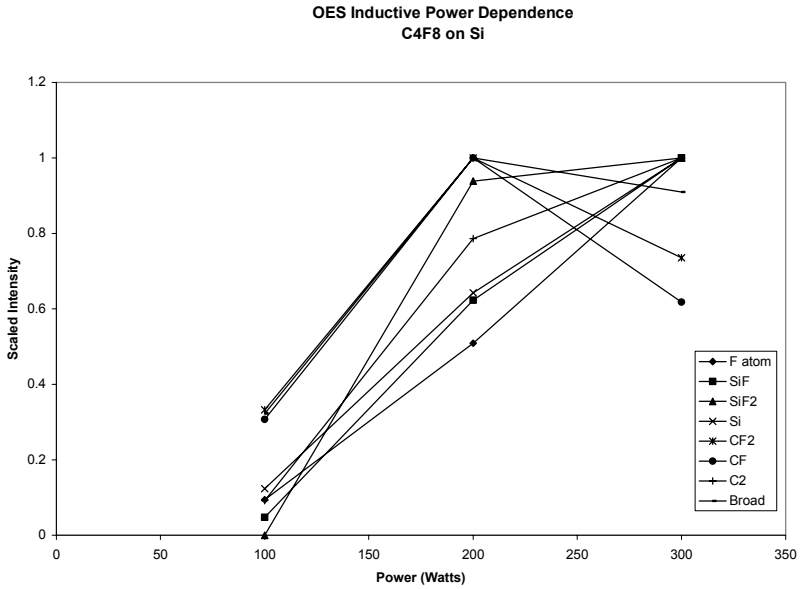
OES Inductive Power Dependence
C4F8 on Si
Scaled Intensity
Power (Watts)
F atom
SiF
SiF2
Si
CF2
CF
C2
Broad

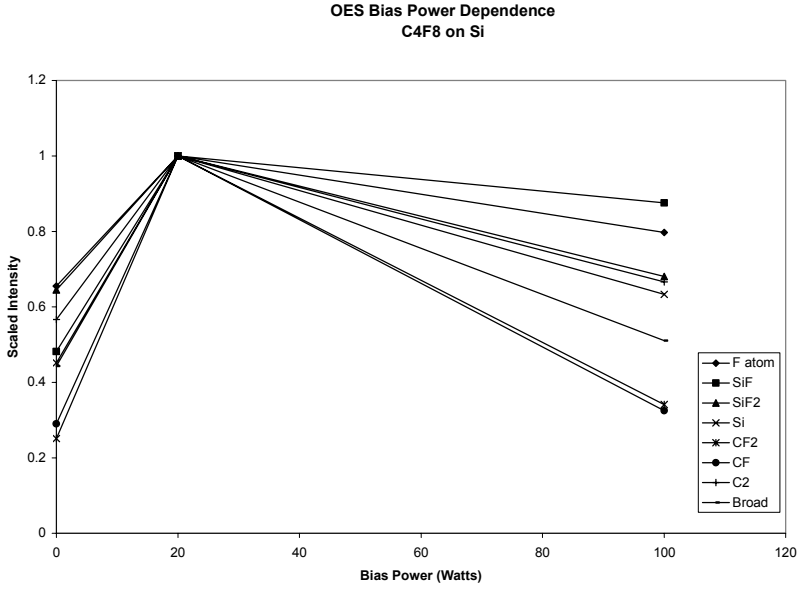
OES Bias Power Dependence
C4F8 on Si
Scaled Intensity
Bias Power (Watts)
F atom
SiF
SiF2
Si
CF2
CF
C2
Broad

C_4F_8 Plasma 10 mTorr 200 W ICP coil power 20 W rf-bias power quartz wafer

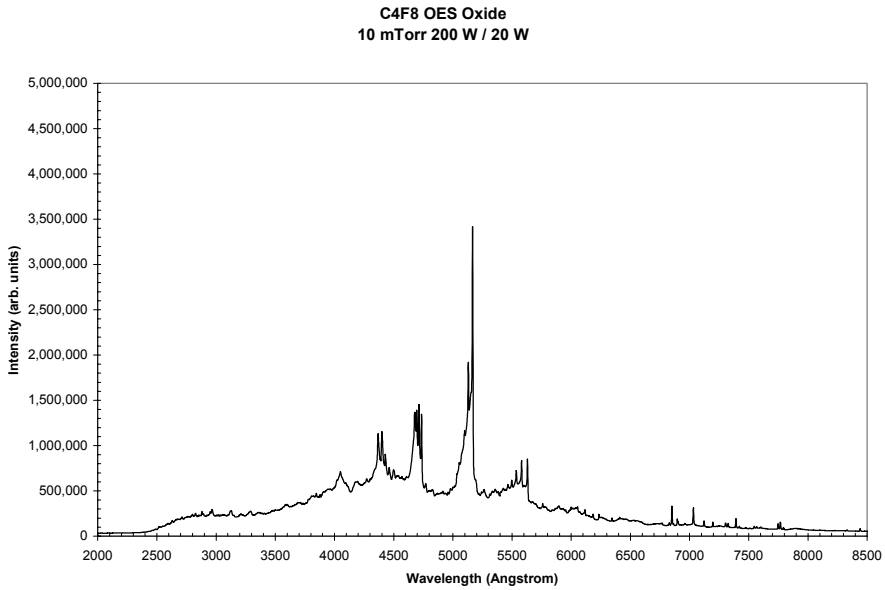

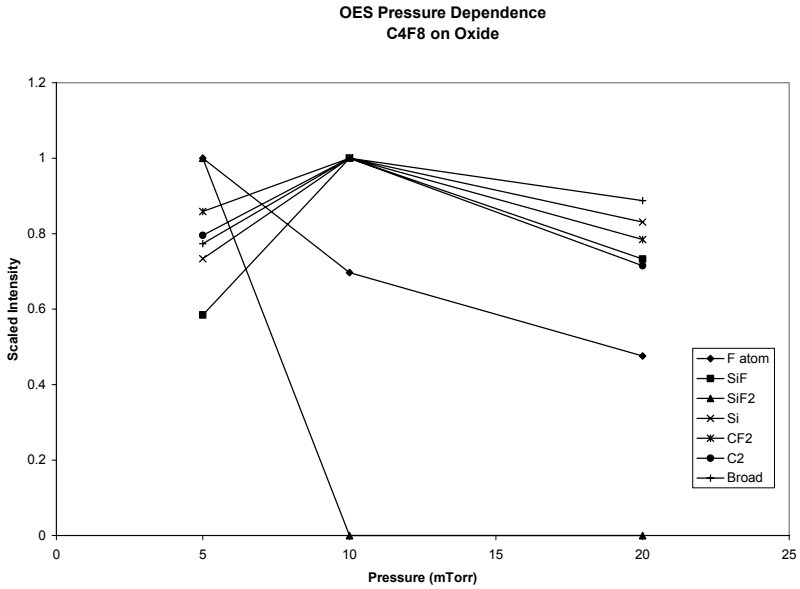

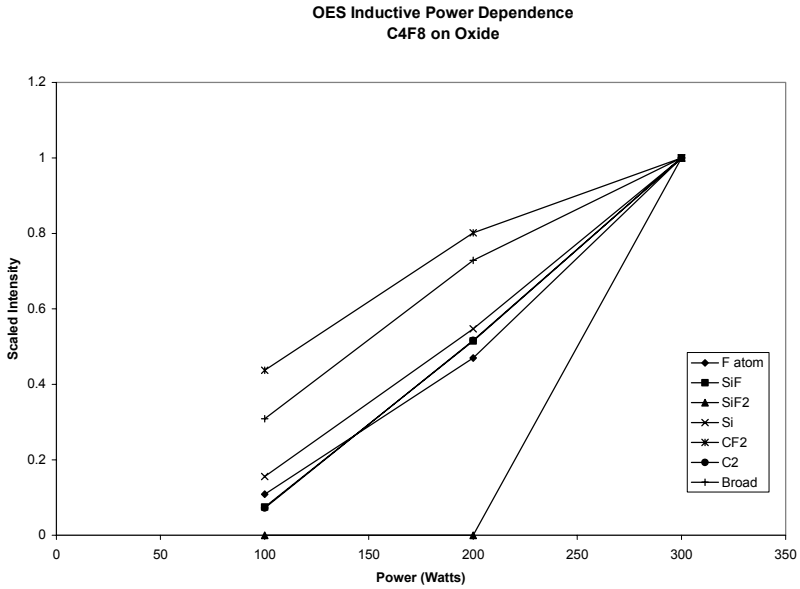
OES Inductive Power Dependence
C4F8 on Oxide
Scaled Intensity
Power (Watts)
1.2
1
0.8
0.6
0.4
0.2
0
0
50
100
150
200
250
300
350
F atom
SiF
SiF2
Si
CF2
C2
Broad

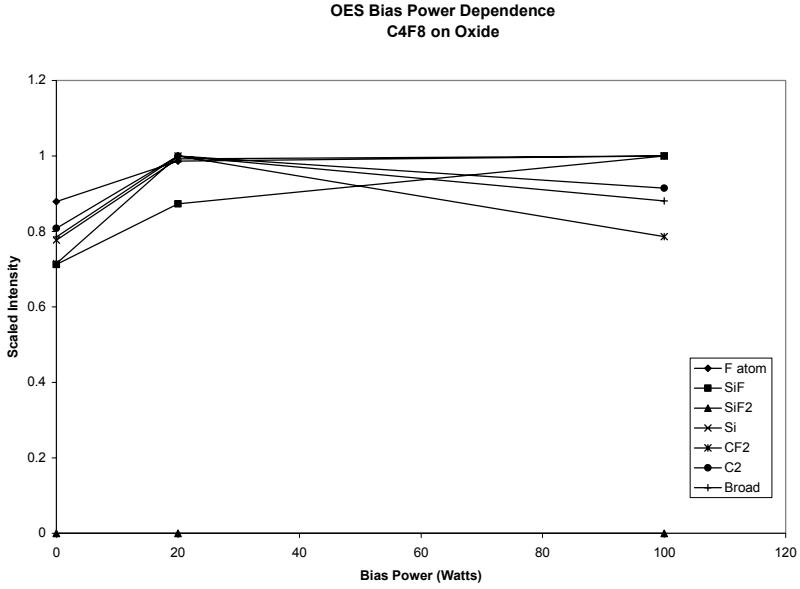
OES Bias Power Dependence
C4F8 on Oxide
Scaled Intensity
Bias Power (Watts)
1.2
1
0.8
0.6
0.4
0.2
0
0
20
40
60
80
100
120
F atom
SiF
SiF2
Si
CF2
C2
Broad

Appendix 2

Mass Spectrometer / Ion Energy Analyzer Measurements in Ar/SF_6 Discharges

Experimental Conditions

The experiments were performed in the GEC Reference Cell. The Cell had the anodized Al ICP window holder and the fused silica ring in place. The Balzers mass spectrometer had a 25 μm pinhole installed. The Balzers instrument can scan either across a mass or energy range, but not both at the same time. This means that for a mass scan of ions, a given ion energy had to be selected.

The data is shown in the next 17 pages. For the mass scan surveys of ions and neutrals, the conditions were 15 mTorr total pressure, 200 W ICP coil power, and 30 W of chuck power, both at 13.56 MHz and phase locked to each other. The applied rf-bias power to the chuck produced an applied voltage of 63 Vpp, as measured by a capacitive voltage sensor. A 6" silicon wafer (with a 1 cm diameter hole in the center) was placed on the chuck during these experiments. For the mass scans of ions, the energy analyzer was set for 40 eV ions. Three mixtures of $Ar/SF_6/O_2$ were surveyed: 50/45/5, 50/25/25, and 0/90/10, with 20 sccm total flowrate. For the mass scan of neutrals, the total flow rate was again 20 sccm and the mixtures of $Ar/SF_6/O_2$ investigated were 50/45/5, 50/25/25, and 90/10/0. Ion energy distributions were measured for the 50/45/5 mixture for SF^+, SF_3^+, and SF_5^+. The neutral molecules were ionized in the spectrometer with a 100 eV electron beam prior to detection.

Relative total ion fluxes of Ar^+ and SF_x^+ (x = 1-5) ions were measured at 10 mTorr total pressure, and 240 W and 360 W ICP coil power for mixtures of 50/50 and 90/10 Ar/SF6 and 10 sccm total flow rate using a 2 mm thick fused silica (SiO_2) wafer, in order to minimize etching. Only a small rf-bias (2 W) was applied to the chuck in order to prevent sulfur deposits on the chuck and pinhole. The experiment was repeated at 240 W ICP coil power twice for the 50/50 Ar/SF_6 mixture and once for the 90/10 mix. A similar experiment was carried out using a silicon wafer and the 90/10 mix at 240 W and 360 W ICP coil power, again at 10 mTorr total pressure and 10 sccm total flow rate. For the silicon wafer experiment, the data includes relative fluxes of the etch products SiF_x^+ (x = 1,2).

Ions, 40 eV $Ar/SF_6/O_2$ 50/45/5

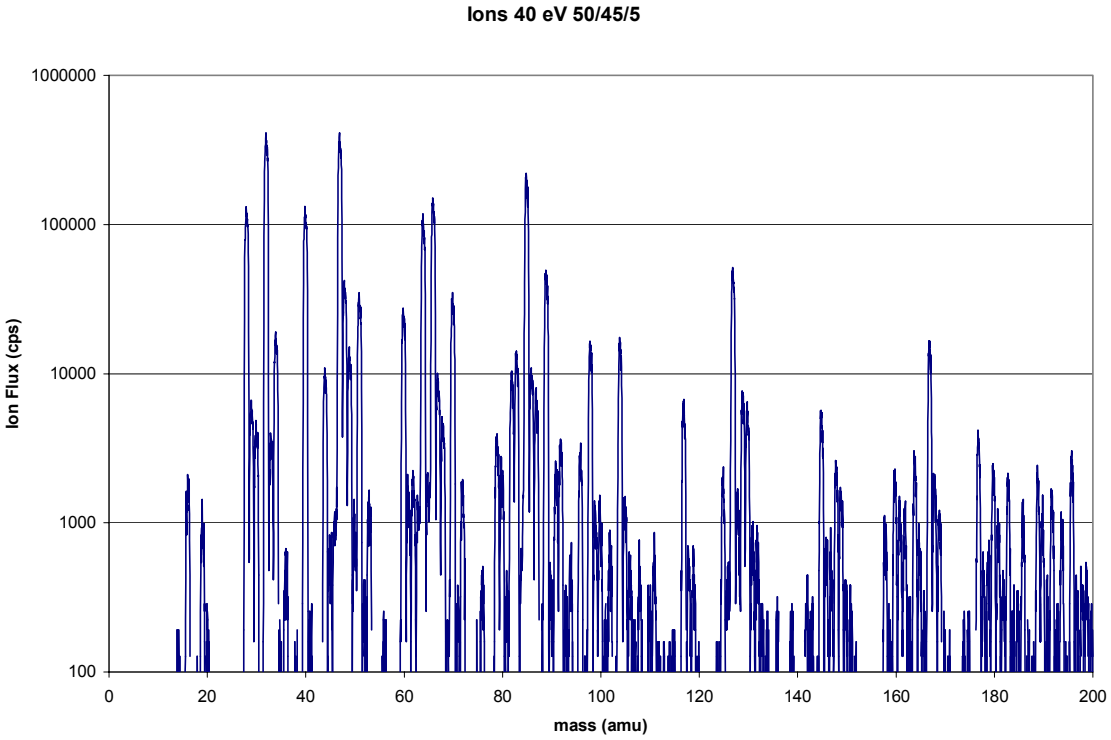

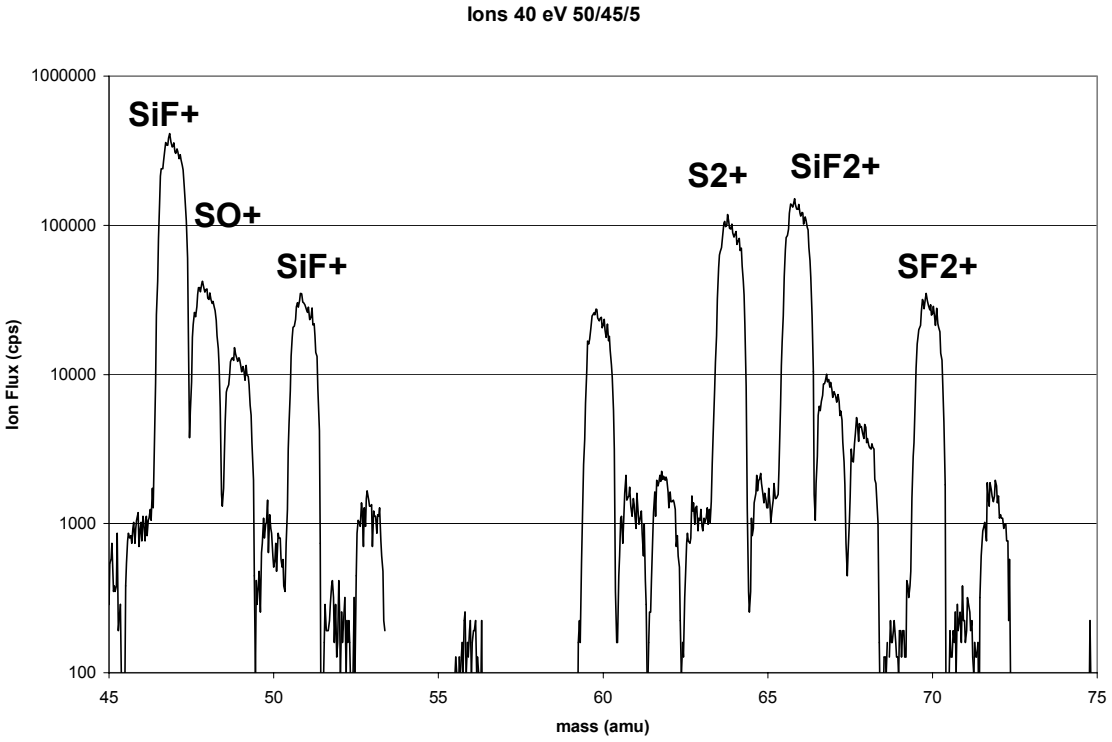
Ions 40 eV 50/45/5
SiF+
SO+
SiF+
S2+
SiF2+
SF2+
Ion Flux (cps)
1000000
100000
10000
1000
100
45
50
55
60
65
70
75
mass (amu)

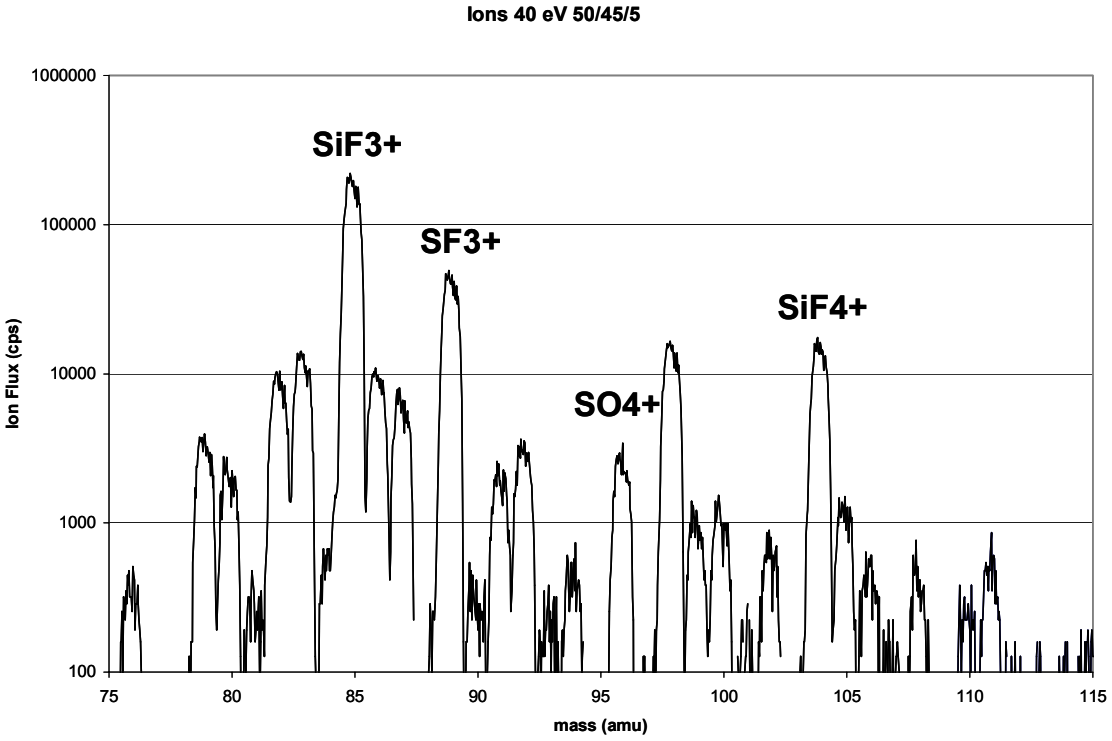
Ions 40 eV 50/45/5
SiF3+
SF3+
SiF4+
SO4+
Ion Flux (cps)
1000000
100000
10000
1000
100
75
80
85
90
95
100
105
110
115
mass (amu)

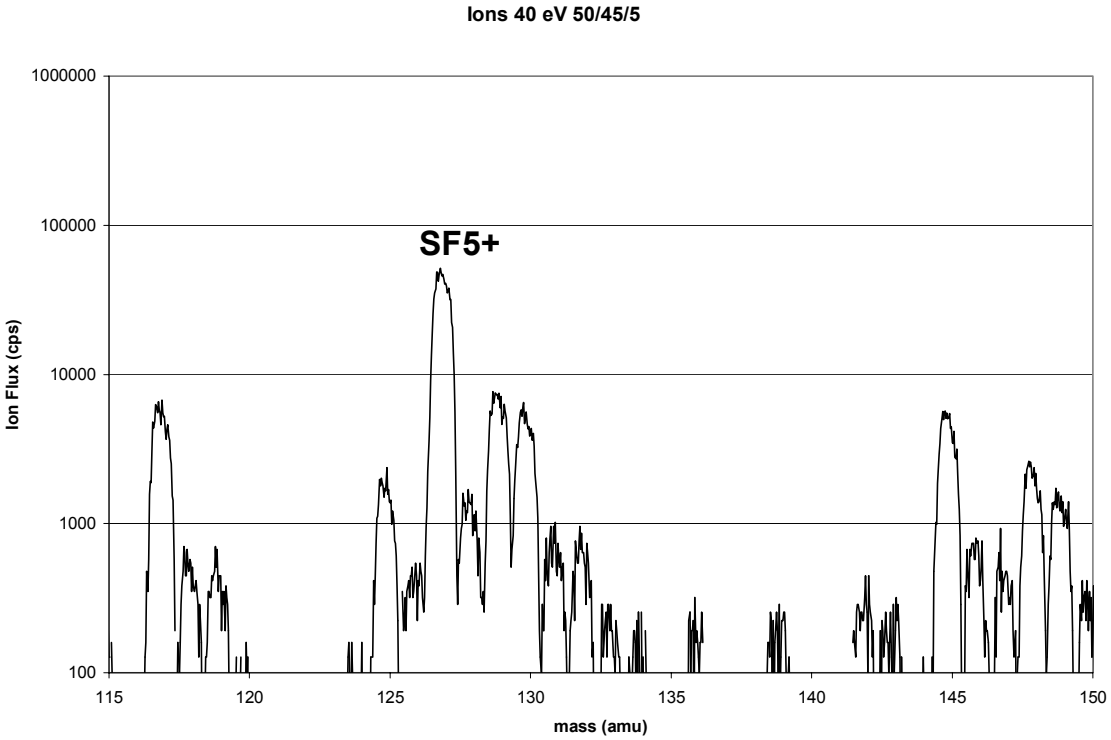
Ions 40 eV 50/45/5
SF5+
Ion Flux (cps)
1000000
100000
10000
1000
100
115
120
125
130
135
140
145
150
mass (amu)

Ions, 40 eV $Ar/SF_6/O_2$ 50/25/25

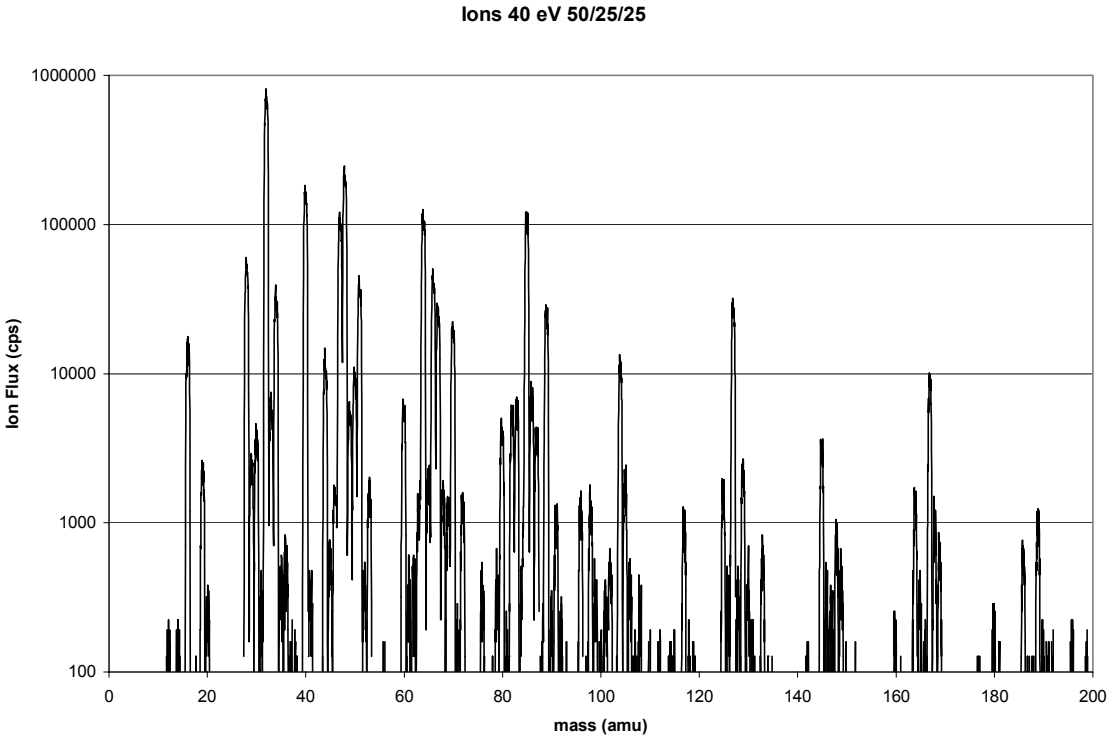

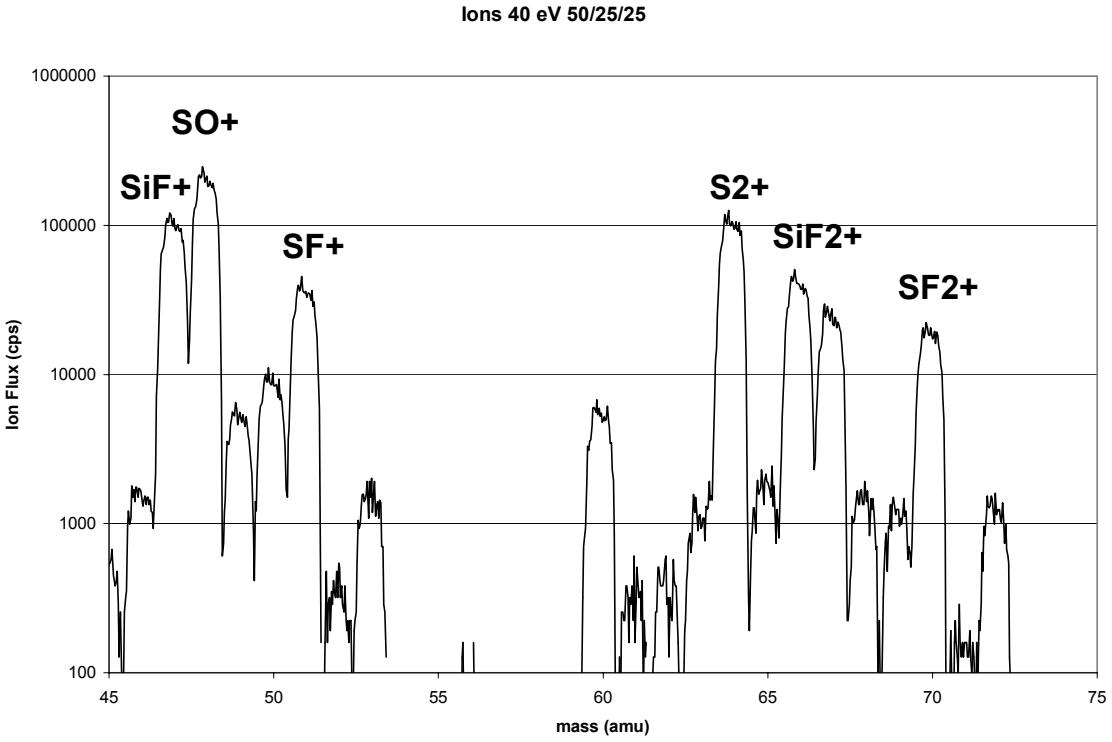
Ions 40 eV 50/25/25
1000000
100000
10000
1000
100
Ion Flux (cps)
SO+
SiF+
SF+
S2+
SiF2+
SF2+
45
50
55
60
65
70
75
mass (amu)

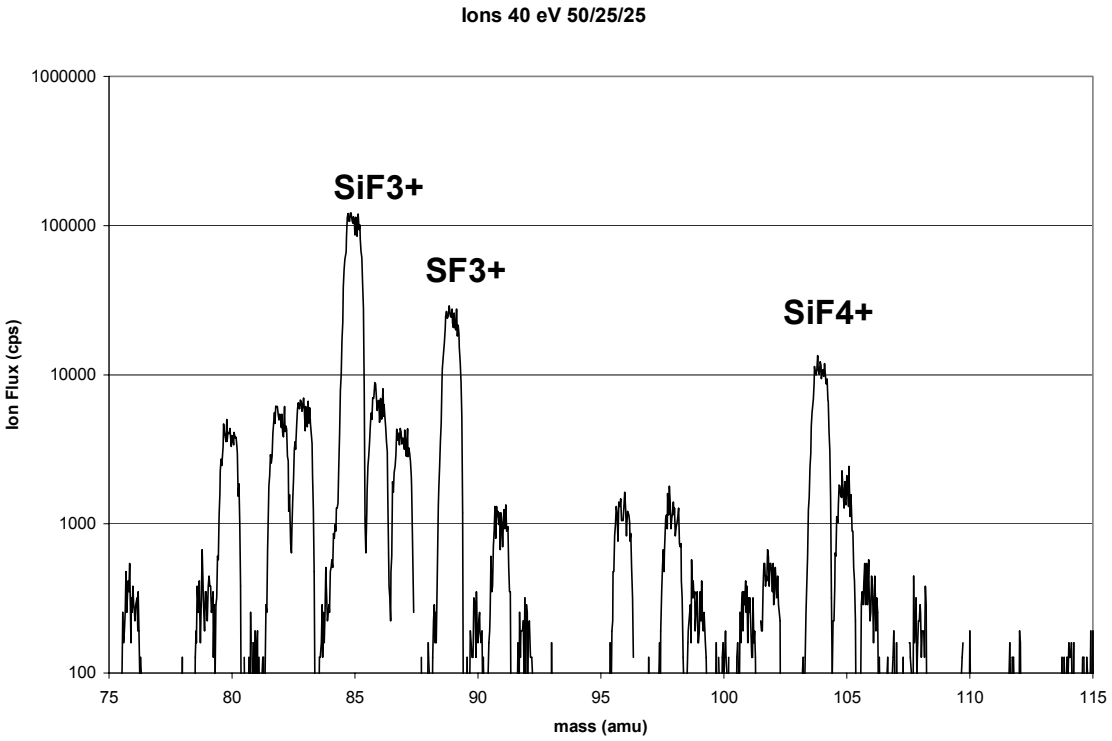
Ions 40 eV 50/25/25
1000000
100000
10000
1000
100
Ion Flux (cps)
SiF3+
SF3+
SiF4+
75
80
85
90
95
100
105
110
115
mass (amu)

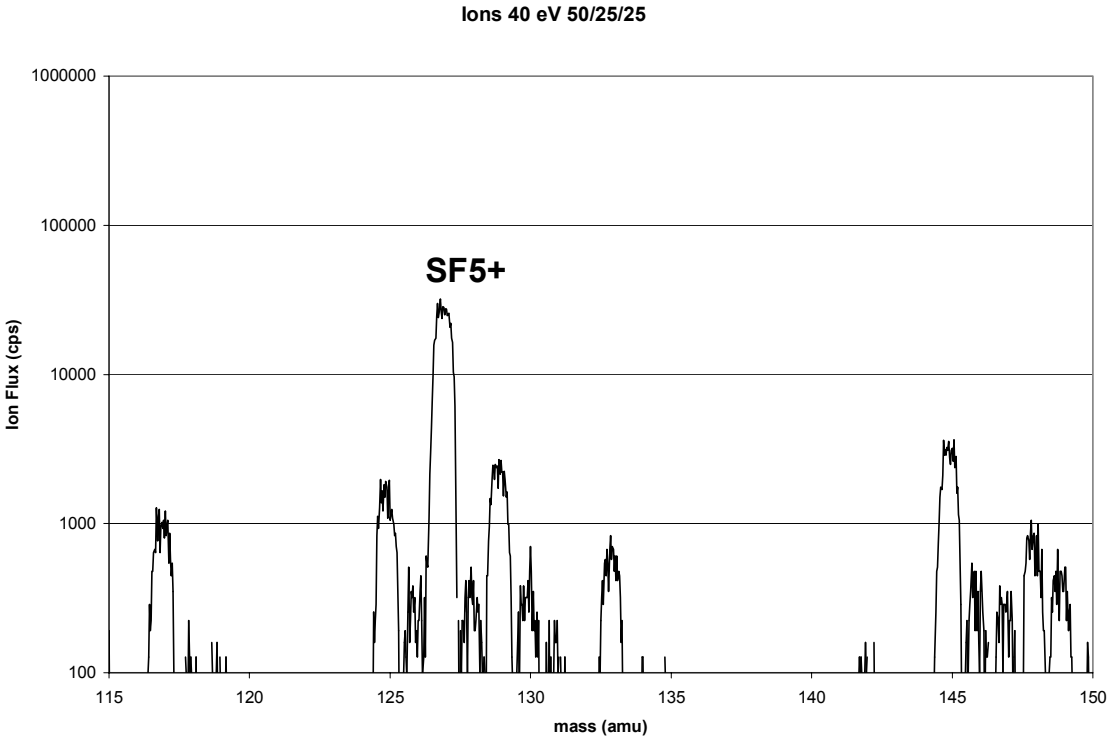
Ions 40 eV 50/25/25
SF5+
Ion Flux (cps)
1000000
100000
10000
1000
100
115
120
125
130
135
140
145
150
mass (amu)

Ions, 40 eV $Ar/SF_6/O_2$ 0/90/10

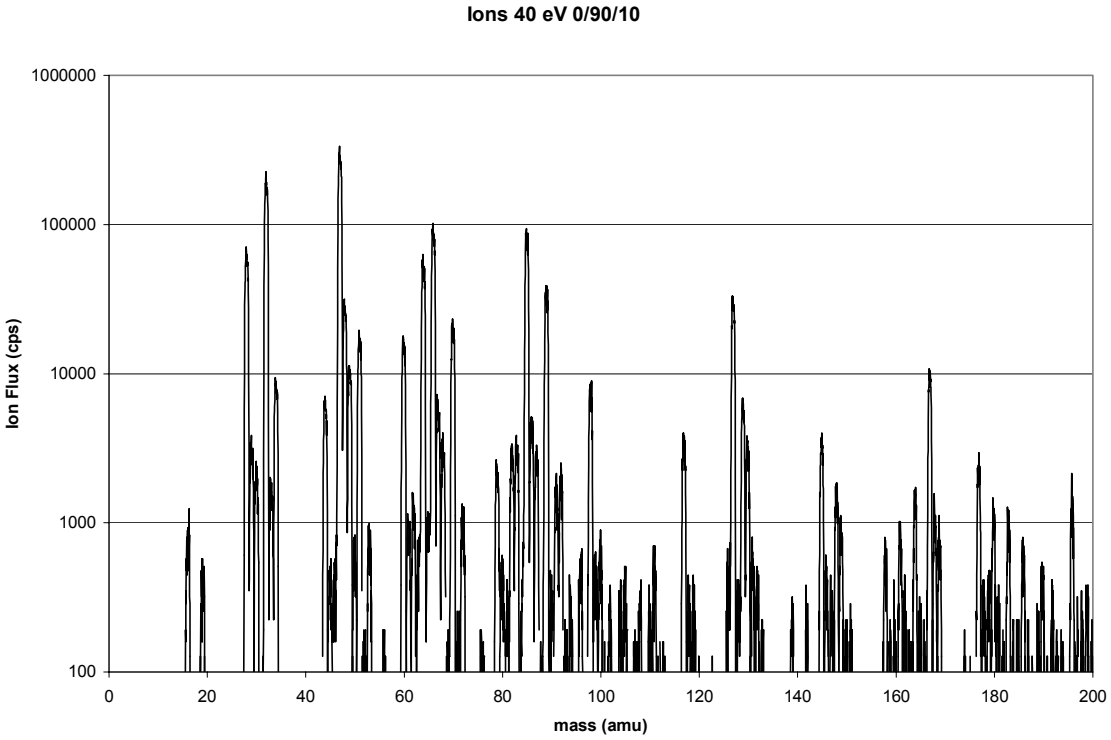

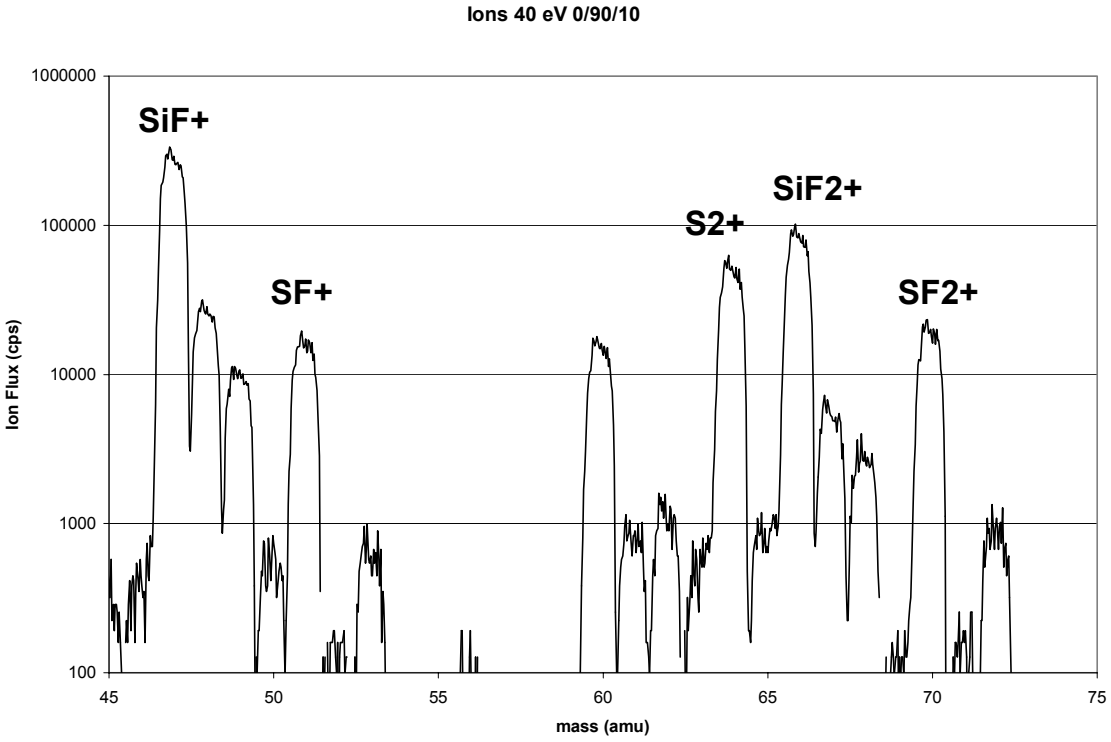
Ions 40 eV 0/90/10
1000000
100000
10000
1000
100
Ion Flux (cps)
SiF+
SF+
S2+
SiF2+
SF2+
45
50
55
60
65
70
75
mass (amu)

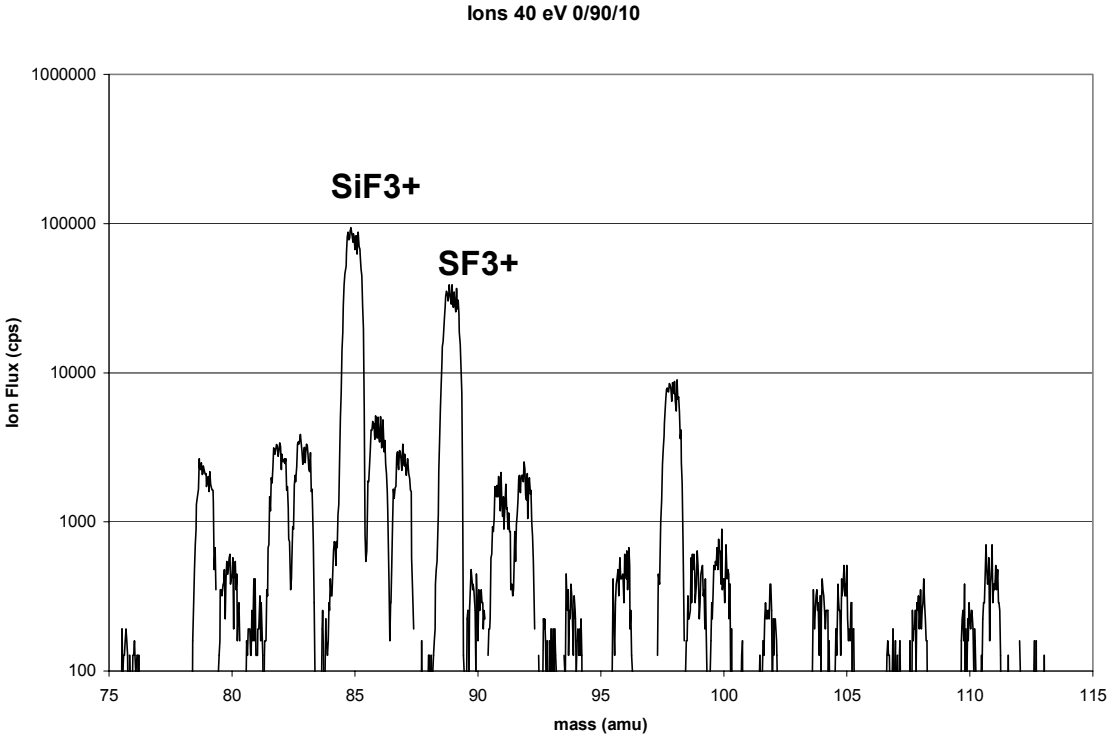
Ions 40 eV 0/90/10
1000000
100000
10000
1000
100
Ion Flux (cps)
SiF3+
SF3+
75
80
85
90
95
100
105
110
115
mass (amu)

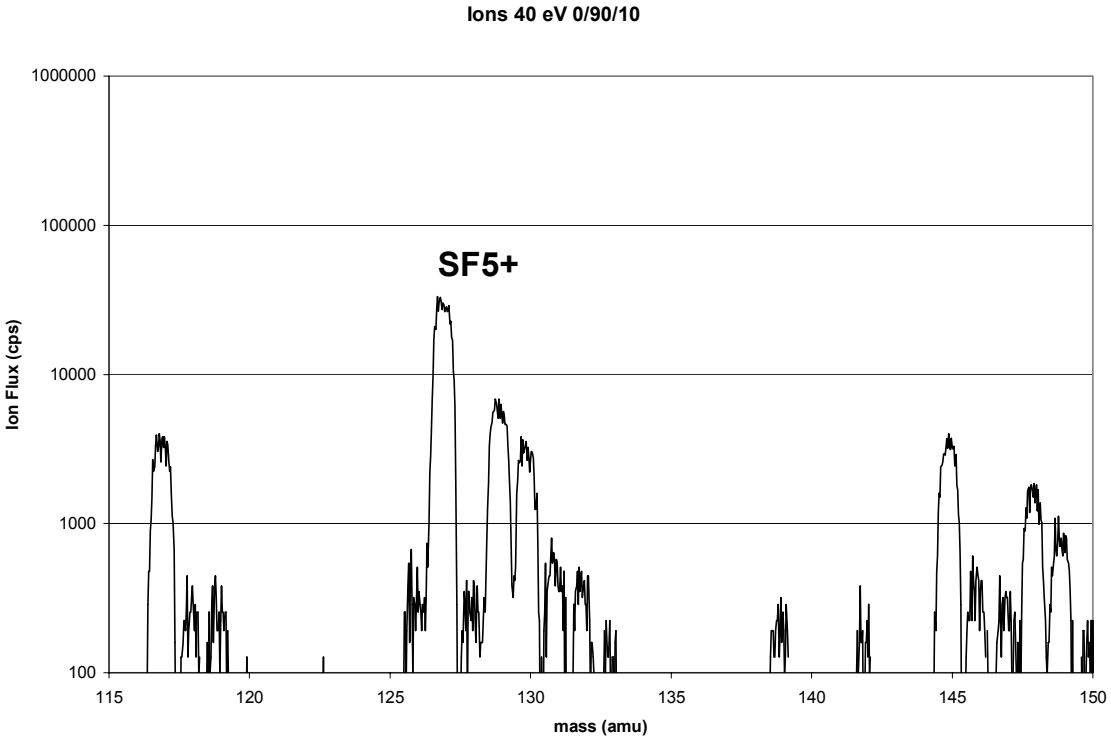
Ions 40 eV 0/90/10
SF5+
Ion Flux (cps)
1000000
100000
10000
1000
100
115
120
125
130
135
140
145
150
mass (amu)

Neutrals $Ar/SF_6/O_2$ 50/45/5

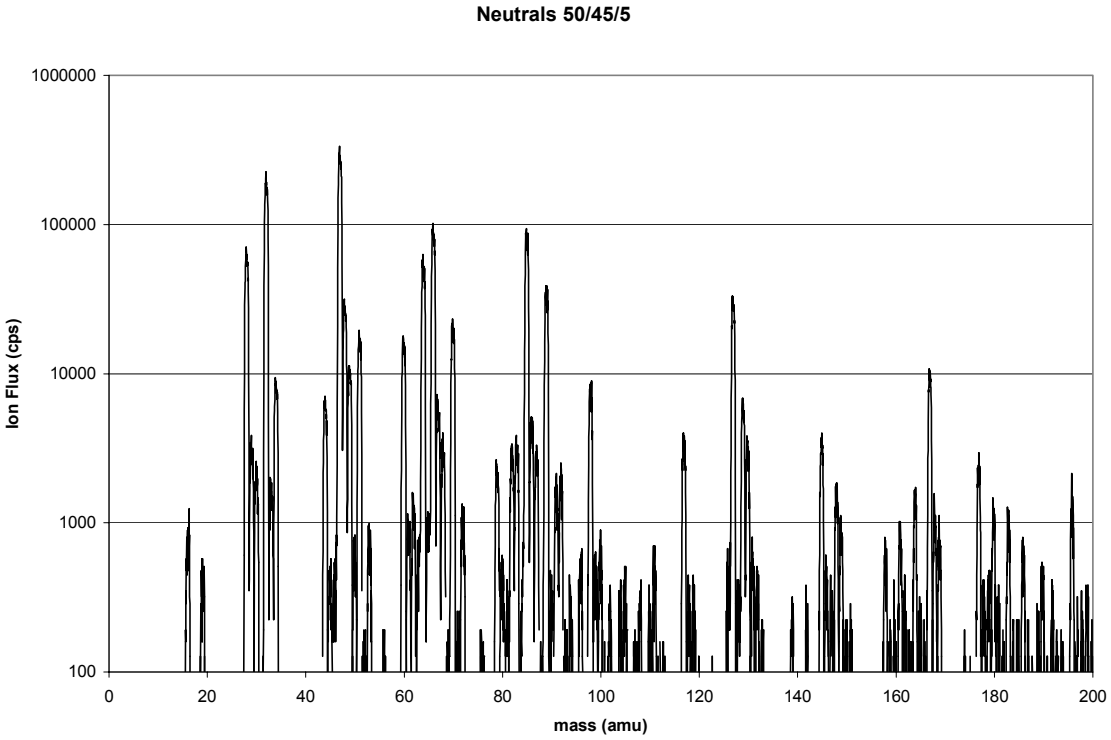

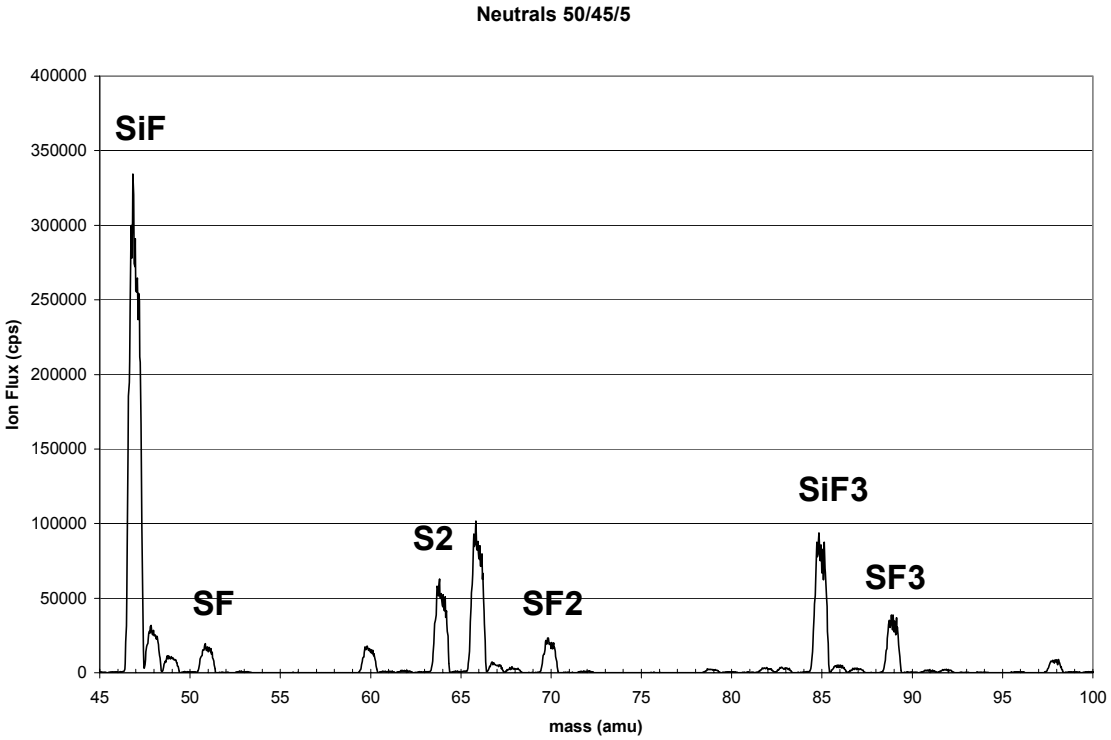
Neutrals 50/45/5
Ion Flux (cps)
400000
350000
300000
250000
200000
150000
100000
50000
0
45
50
55
60
65
70
75
80
85
90
95
100
mass (amu)
SiF
SF
S2
SF2
SiF3
SF3

Neutrals $Ar/SF_6/O_2$ 50/25/25

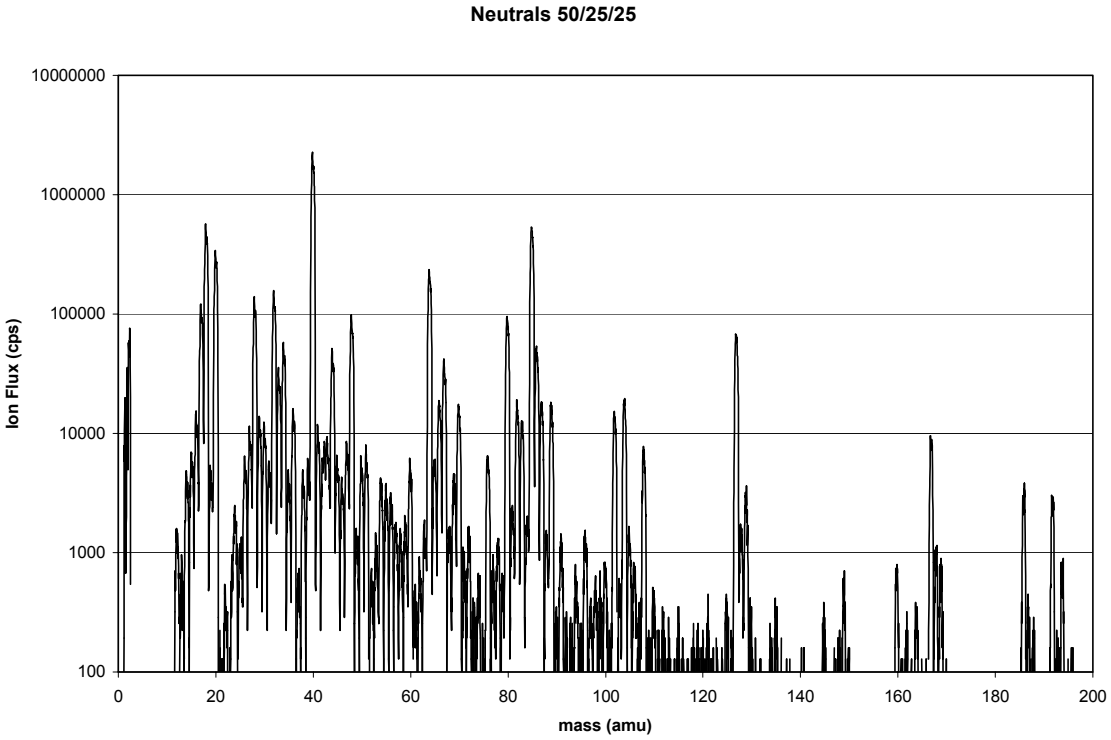

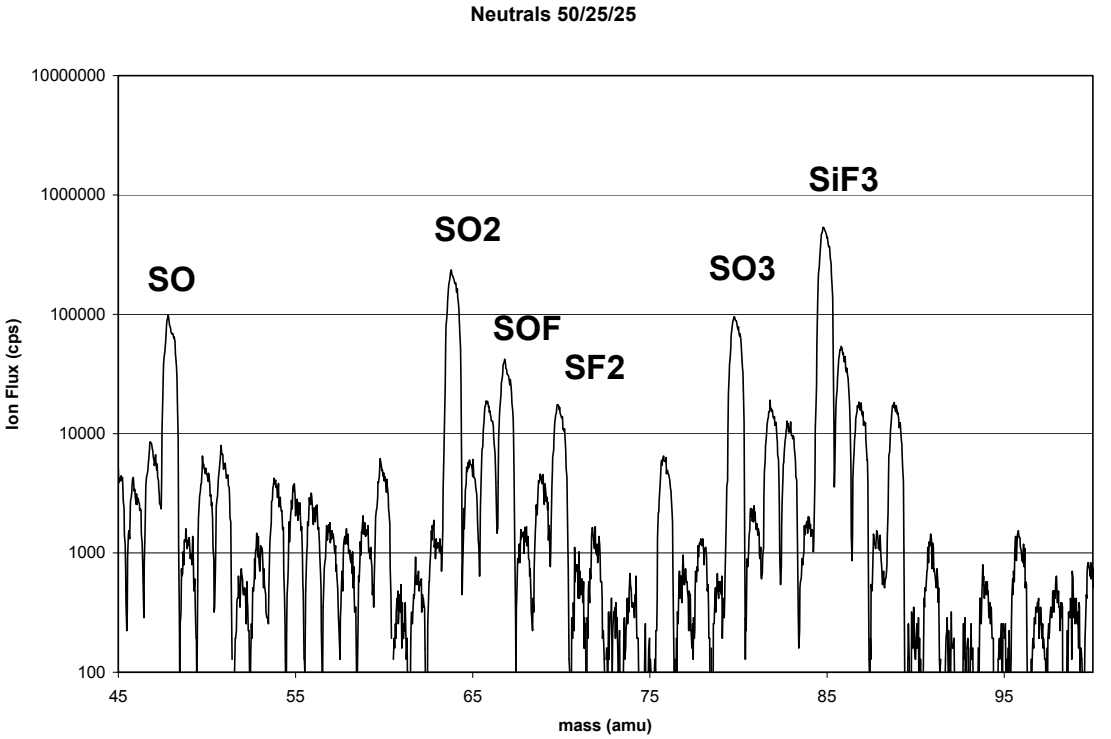

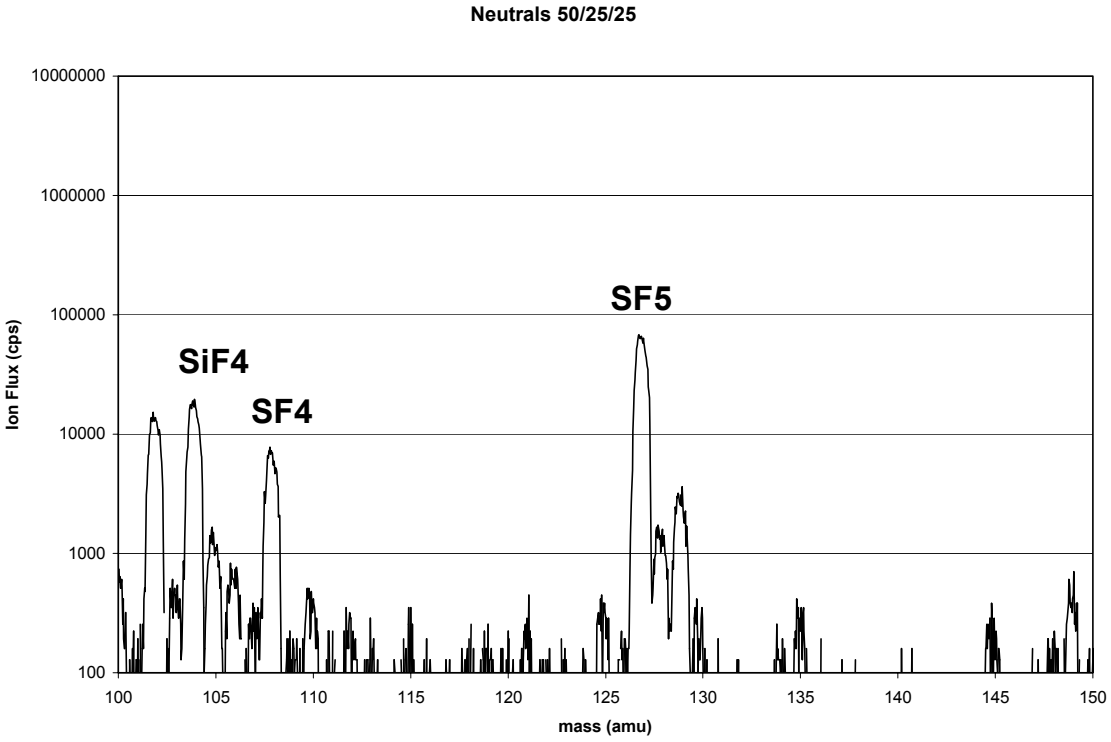

Neutrals $Ar/SF_6/O_2$ 90/10/0

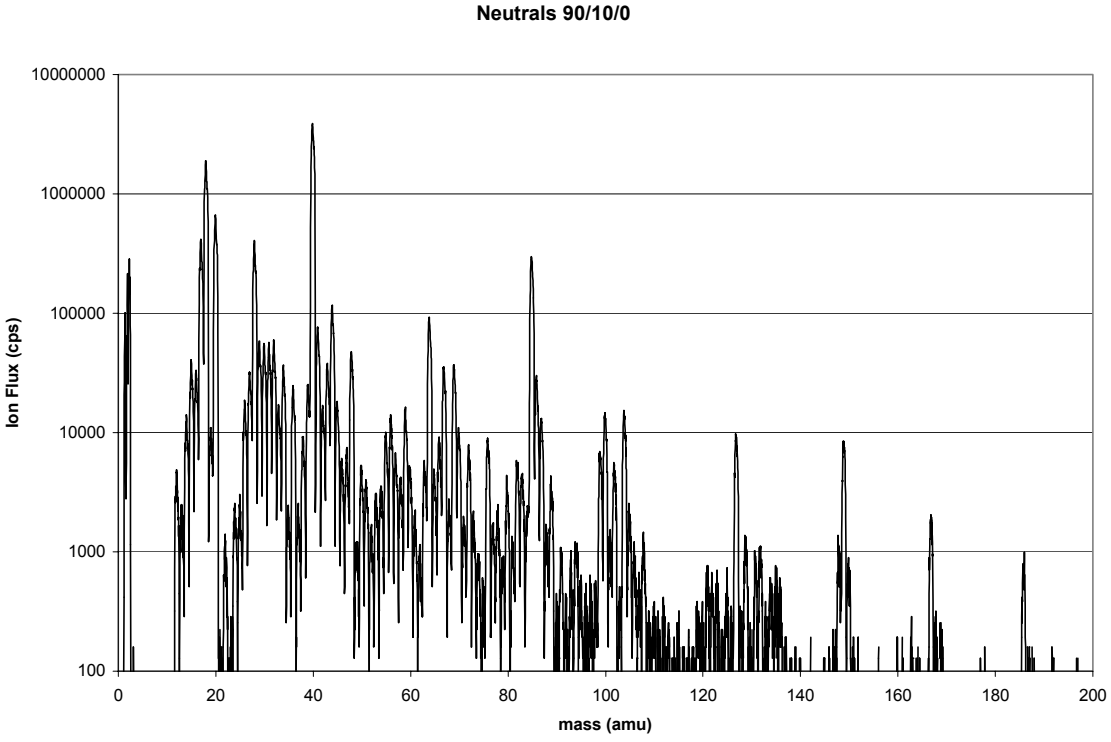

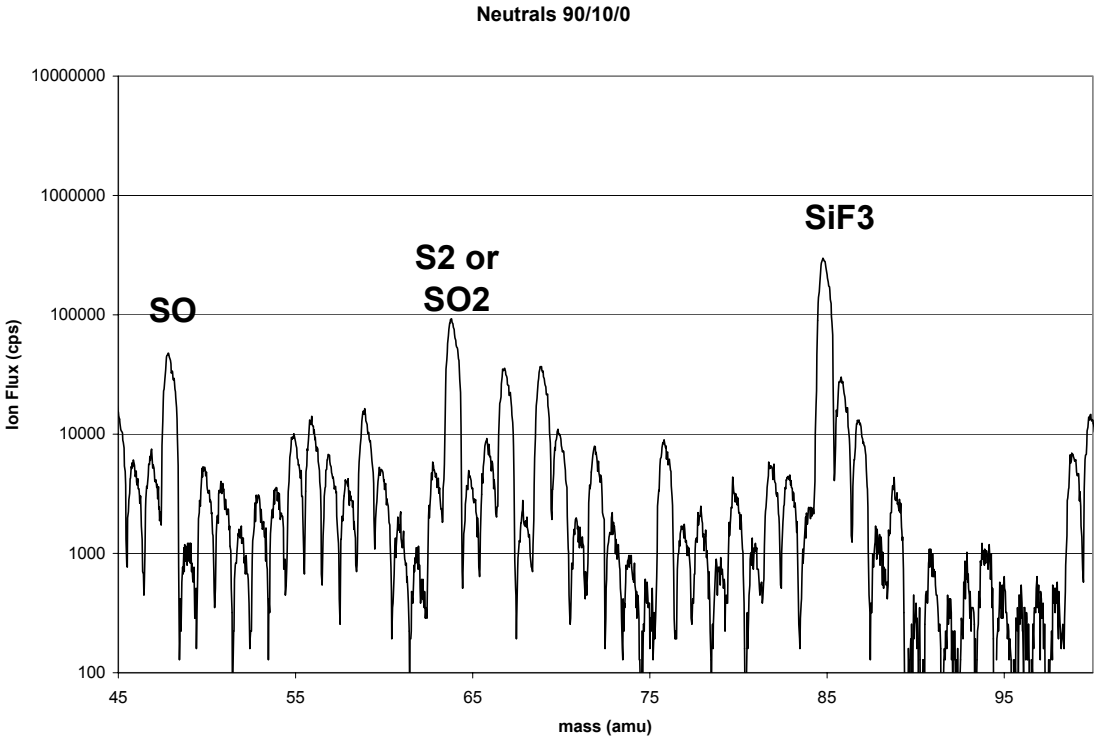
Neutrals 90/10/0
10000000
1000000
100000
10000
1000
100
Ion Flux (cps)
SO
S2 or
SO2
SiF3
45
55
65
75
85
95
mass (amu)

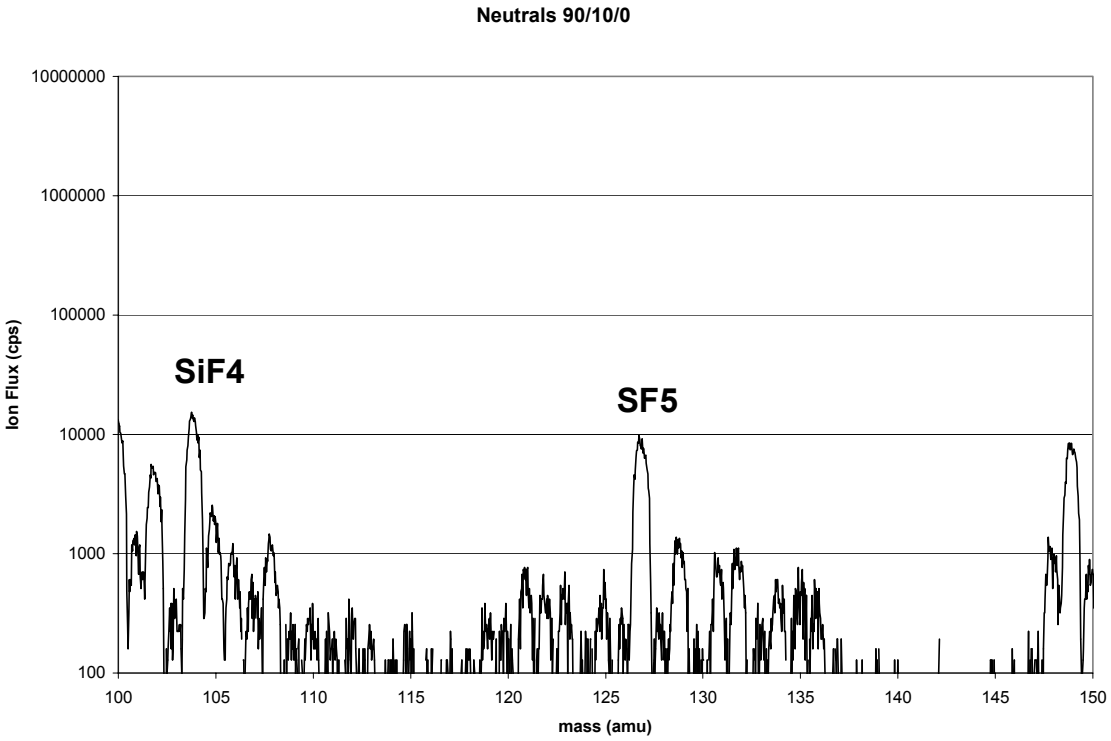
Neutrals 90/10/0
10000000
1000000
100000
10000
1000
100
Ion Flux (cps)
SiF4
SF5
100
105
110
115
120
125
130
135
140
145
150
mass (amu)

Relative Ion Flux SiO_2 Wafer

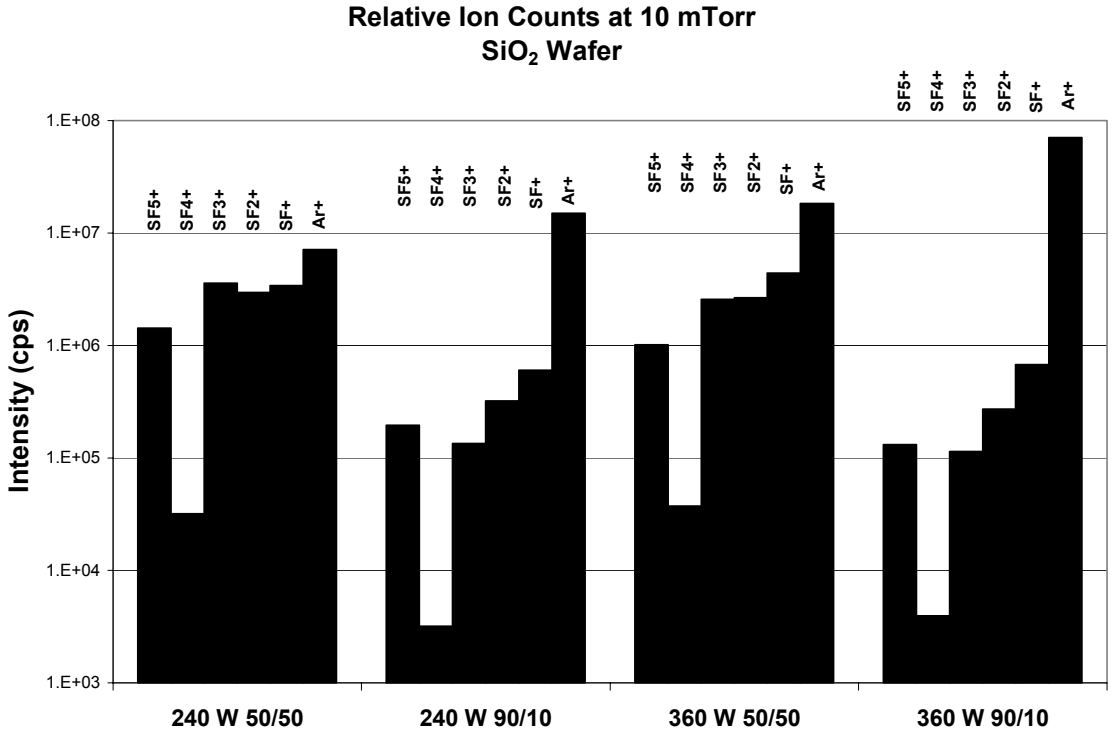

Relative Ion Flux SiO_2 Wafer Repeat

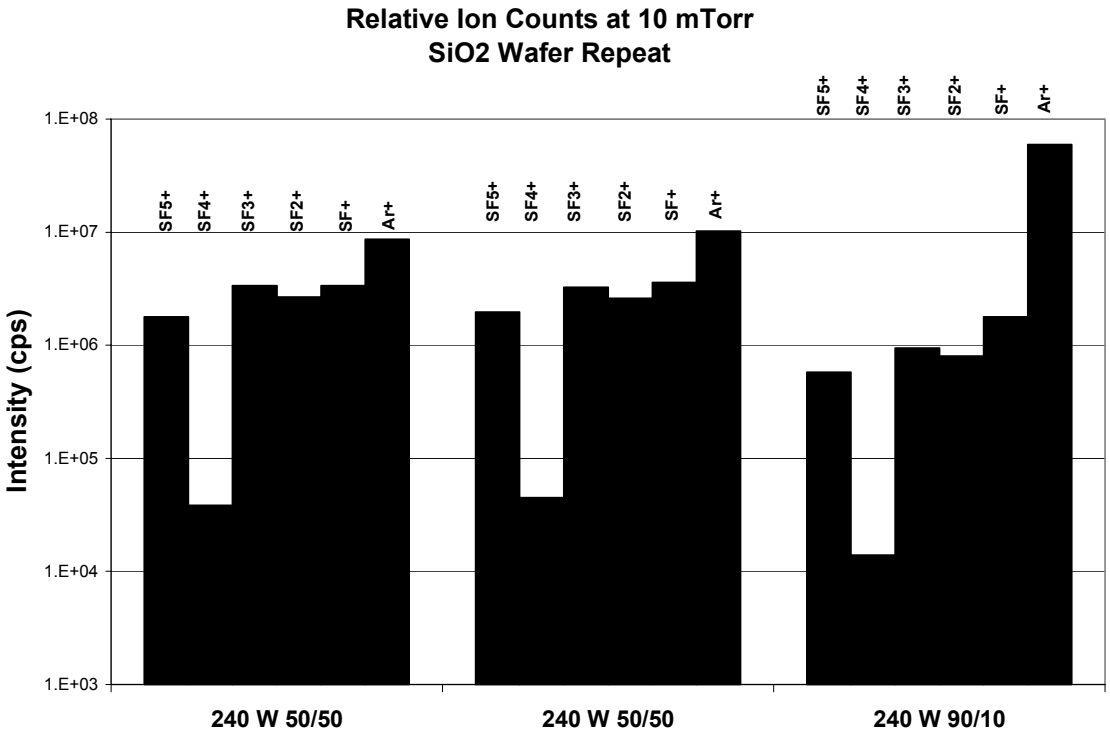

Relative Ion Flux Si Wafer

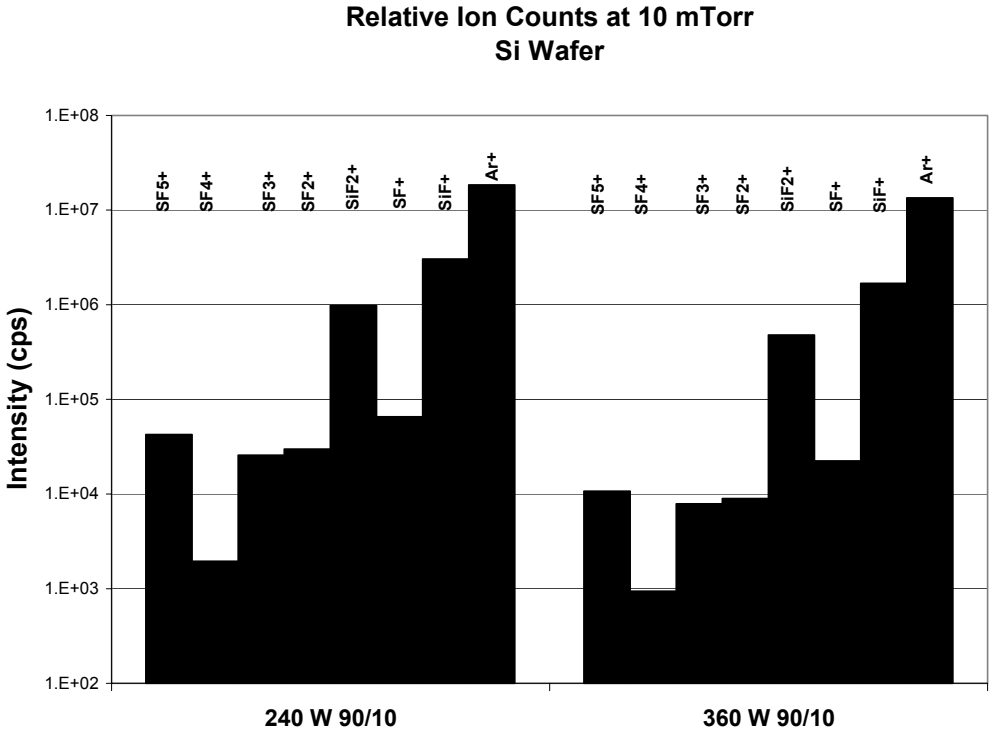

SF_x^+ Ion Energy Distributions $Ar/SF_6/O_2$ 50/45/5

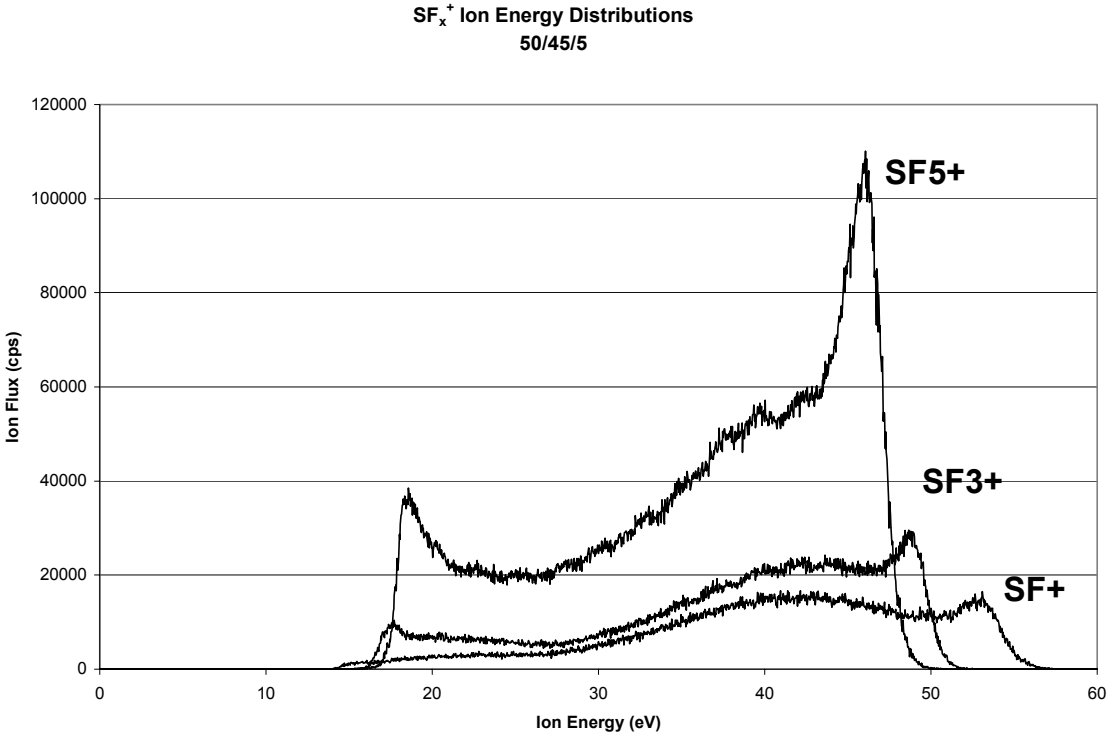

Appendix 3

Surface dependent electron and negative ion density in SF_6 / Argon gas mixtures

I. Introduction

Electrically driven plasmas containing halogens are commonly used in a number of material modification and surface cleaning processes. For example, discharges containing SF_6 and the many varieties of fluorocarbon gases, $C_xF_yH_z$, are used to etch silicon or silicon dioxide for microelectronic feature definition. These gases serve as rich sources of atomic fluorine to etch material. In addition, the fluorocarbon gases also supply C_xF_y radicals for sidewall passivation and protection during deep trench etching. However, in cases where sidewall passivation is not required or is provided by another process, the use of SF_6 is common, as in the Bosch process.[1]

To understand the critical chemical mechanisms in negative ion containing plasmas, it is important to determine both the electron and negative ion densities. In such plasmas, the electron and negative ion density are fundamental plasma parameters that are influenced by a number of gas and surface reactions. Negative ion formation serves as a loss mechanism for electrons, and because negative ions tend to collect in regions of maximum plasma potential, they can serve as a significant loss term for volumetric ion-ion recombination with positive ions. Negative ions can also influence the sheath voltage and kinetics, and in the case of pulsed discharge systems, possibly influence the surface charge. At a more fundamental level, electron and negative ion interactions can alter the electron energy distribution function, affect the spatial distribution of the plasma potential, and by charge neutrality, influence the total positive ion charge density. This in turn can impact the ion flux and ion energy to the wafer surface. Finally, measurements of the electron and negative ion densities can be used, along with

additional measurements, to benchmark and validate recent computer models and to test radical species chemical reaction mechanisms.[2]

A key aspect of most plasma processes is that some type of work, such as etching or cleaning, is done at the plasma / surface boundary layer. As understanding of the important processes that occur at the plasma / surface boundary layer has improved, we now realize that etch product chemistry must also be included in both experiments and models to capture a complete picture of surface profile evolution. For example, a typical etch rate of 500 nm / min translates into a etch product gas flow from the surface of approximately 40 sccm for an 8 inch diameter wafer. A gas flow of 40 sccm is a significant fraction of the total gas flow rate in most processing tools. Radical species that are evolved from the surface into the gas phase will fully participate in the myriad of gas phase and surface reactions that are associated with the parent fluorocarbon gas. Those processes include negative ion formation, electron dissociation, ionization which contributes to the charge balance, molecular quenching of the electron temperature, and ion surface bombardment. Thus it is important that more experiments focus on the influence of surface material and that models begin to incorporate etch products in a self consistent manner. This clearly increases the complexity of the problem but is the only way to capture all of the appropriate physics.

There have been a number of measurements of the electron and negative ion density in SF_6, although few reported in inductively driven plasmas (ICP).[3,4,5,6,7,8] Kimura and Ohe recently reported probe measurements in SF_6 / Xe gas mixtures in an ICP.[3] They reported electron densities on the order of 5×10^{10} cm^{-3} , and negative ion densities approximately 5 times higher at moderate powers of 80 W. Kono and coworkers measured the electron and negative ion density in a capacitively coupled

parallel plate chamber using a microwave cavity technique and laser photodetachment.[4] At relatively low input powers of 10 W and pressures of less than 100 mTorr, they measured electron densities on the order of 10^9 cm^{-3} and negative ion densities a factor of 100 higher. St-Onge and coworkers performed laser photodetachment measurements in SF_6 containing magnetoplasmas.[5] They measured a negative ion / electron density ratio of 2 to 5 for pressures of 0.2 to 4 mTorr in the region downstream from their microwave source. This work also includes a good description of the challenges associated with accurate negative ion identification and the subsequent assignment of absolute densities to the measured photodetachment signal.

This investigation is an extension of our recent measurements of the electron and negative ion density in inductively driven discharges containing C_2F_6, CHF_3, and C_4F_8 [9,10] The current work focuses on electron and negative ion densities in SF_6 / Ar gas mixtures as well as voltage and current measurements. We study power densities in the range of 0.1 to 1 W/cm^3 where molecular disassociation tends to be larger than previous work. In addition to measuring the electron and negative ion density in SF_6 / Ar gas mixtures, this study also investigated the influence of surface material on the electron and negative ion density. The rf biased wafer surface was covered with either a bare silicon wafer or a 1-mm-thick fused silica wafer to provide a uniform SiO_2 surface. Our previous work in Cl_2 / BCl_3, and C_4F_8 containing discharges showed significant differences in the electron and negative ion densities above different surface materials.[10,11]

II. Experimental setup

Experiments were performed in a Gaseous Electronics Conference (GEC) rf reference cell which was modified to include an inductively coupled plasma (ICP) source.[12,13] Briefly, the induction coil was constructed from 3.2 mm diameter copper tubing which was wound into a five-turn planar coil 11 cm in diameter, and was water cooled. In this work, the coil was excited at 13.56 MHz. The coil was separated from the plasma by a 1-cm-thick fused silica window. The spacing between the window and the lower electrode was 3.8 cm. For these experiments, the lower electrode was rf biased (13.56 MHz) and covered with either a 6 inch diameter, 0.6 mm thick, silicon wafer or a 6 inch diameter, 1 mm thick, fused silica (SiO_2) wafer. The wafers rested on the lower electrode without clamping. The lower electrode was water cooled; however, the reactor was run with a discharge (SF_6 or O_2) for 30 minutes to reach a steady-state temperature and wall condition before any measurements were made. For these experiments an additional modification was made to the GEC chamber; a fused silica ring was clamped to the upper electrode assembly. The fused silica confinement ring served to stabilize and extend the operating parameter space of the electronegative discharges. Without the ring in place, the discharge could only be sustained over a narrow range of power and pressure. The ring had an inner diameter of 4.5 inches, outer diameter of 6.5 inches and a thickness of 0.75 inches. In addition, the standard stainless steel ICP window holder was replaced by an anodized aluminum holder so that the materials in contact with the plasma would more closely resemble those found in commercial tools.

Line integrated electron density was measured using a microwave interferometer, while the absolute negative ion density in the center of the plasma was inferred from a laser photodetachment measurement. The equipment and experimental configuration were identical to that described in previous studies of the electron and negative ion

density in Cl_2, BCl_3, C_2F_6, CHF_3 and C_4F_8 containing inductive discharges.[9,10,11,14,15] The microwave interferometer operated at 80 GHz, and standard, high gain horns and microwave lenses were used to transmit the microwaves through the plasma. The reported *line-integrated* electron density can be converted into the electron density in the center of the plasma by dividing the line-integrated density by an effective path length of 10 cm.[12]

Negative-ion laser-photodetachment experiments were performed using a frequency-quadrupled Nd:YAG laser with typical pulse energy of 20 mJ at 266 nm. In the following analysis, the negative ion was assumed to be F^- with a measured photodetachment cross section of 5×10^{-18} cm^{-2}.[16,17] Unlike our previous measurements in fluorocarbon containing plasmas, the assumption that F^- is the dominant negative ion is subject to some uncertainty due to the likely presence of SF_3^- and SF_5^- in addition to F^-. However, due to the high dissociation at our measured electron densities, the contributions of the molecular negative ions are likely to be modest.[5] Several calibration factors are used to convert the measured excess electron density produced by photodetachment to an absolute negative ion density. First, the spatial distribution of the microwave probe beam must be determined.[18] Second, the spatial energy distribution of the photodetaching laser should be made uniform or be measured. Third, a fractional photodetachment efficiency must be calculated from the measured cross section; any given photon that traverses the plasma may not photodetach an electron from a negative ion.[16,17] For the laser energy used in this experiment, approximately 10 - 30 percent of the F^- was photodetached and the excess electron density was linear in laser energy. Finally, the microwave interferometer and amplifiers must be calibrated. The total uncertainty of these calibrations results in a factor of two uncertainty in the absolute F^-

number density. However, in any given data set (one plot), the *relative* density variation was reproducibly $\pm$10 percent.

III. Results and discussion

A. Electron and negation ion density

Electron and negative ion densities in pure SF_6 and in a 1 / 1 SF_6 / Ar mixture above silicon and silicon dioxide surfaces are shown in Fig. 1 as a function of induction coil power. The pressure was constant at 10 mTorr and the wafer bias power was 20 W. In our plasma chamber, we were unable to generate a plasma in pure SF_6 above a SiO_2 surface. In all cases, the electron density increased linearly with power and the density above the SiO_2 surface was higher than above a Si surface. In addition, the electron density in a 1 / 1 SF_6 / Ar gas mixture was higher than in pure SF_6. A linear increase in electron density with induction coil power has also been observed in a number of other gases in the GEC chamber such as He, Ar, Cl_2, BCl_3, C_2F_6, C_4F_8 and CHF_3.[9,12,14,15] The slope of the increase in electron density with rf power was independent of the SF_6 / Ar ratio but was dependent on the surface material. Thus the gas phase electron production processes ($X + e^- \rightarrow X^+ + 2e^-$) depend on the surface, likely due to changes in the gas phase radical densities due to etching of Si *vs*. SiO_2. In previous measurements of the electron density in fluorocarbon containing plasmas, the electron density was not a strong function of the surface of the biased wafer.[10] It is tempting to assign the difference between SF_6 and C_4F_8 to the surface polymer layer that is produced by fluorocarbon plasmas. In the case of a fluorocarbon plasma, the plasma / surface chemistry is dominated by interactions with the polymer surface layer with apparently minor contributions from the underlying Si or SiO_2 material. In the case of SF_6, there is no

significant surface polymer coverage. Thus the plasma-generated radicals that etch the surface can interact directly with the Si or SiO_2, producing different etch products that in turn result in the differences in the electron density. While a fraction of this argument is likely true, there are a number of other plausible mechanisms that may contribute as well. For example, electron loss by negative ion formation depends on the molecular precursor species and the electron temperature dependencies. In addition, the electron energy distribution function, ionization rate and negative ion formation rate also depend on the gas phase species. Thus further work is required to fully clarify the most important mechanisms.

The negative ion density shown in Fig. 1 also depends on both surface and the SF_6 / Ar gas ratio. The negative ion density was higher above a SiO_2 surface than above a Si surface, as would be expected from the higher electron density. However despite a linear increase in the electron density with power, the negative ion density for the three conditions measured linearly decreased. A linear increase in the electron density would be expected to result in a linear increase in negative ion density if the negative ion formation process is dissociative attachment ($XY + e^- \rightarrow X^- + Y$) and if the concentration or the identity of the precursor species (XY) did not vary with power. However, the negative-ion molecular precursor loss (due to either dissociation or ionization, $XY + e^- \rightarrow X^{(+)} + Y + (2)e^-$) is also a function of the electron density. Thus while the electron density increases, the concentration of the negative ion molecular precursor XY linearly decreases. This would result in an approximately constant negative ion density. The slight decrease in the measured negative ion density could be due to processes such as a change in the gas density due to gas heating,[19] changes in the electron energy distribution function or surface combination.

Comparison of our measurements in SF_6 with prior measurements in SF_6 containing plasmas shows several similarities and differences. Consistent with previous work, we measure a linear increase in the electron density with increased power.[3,4] However, our electron densities are significantly higher than previous measurements, likely due to our plasma (higher W/cm^3 than previous systems) and geometry. The negative ion densities are also higher than most previous measurements but our negative-ion / electron density ratio is less than one, in contrast to most measurements. This is likely due to the higher molecular dissociation that is observed in most ICP discharges and the lack of magnetic confinement, which can modify the electron temperature.

Comparison of our measurements in SF_6 with our previous measurements in fluorocarbon containing plasmas shows several interesting differences. For the case of fluorocarbon etching of Si, we measured a maximum in the negative ion density at an induction coil power of approximately 200 W, which was not observed in SF_6.[9,10] The maximum was attributed to power dependent changes in the concentration of the negative ion precursor species XY, likely the parent gas. A similar maximum was not observed for SiO_2 surfaces during fluorocarbon etching or for the SF_6 data. In our measurement in fluorocarbon containing gas mixtures, the negative ion / electron density ratio was also less than one.

Electron and negative ion densities in pure SF_6 and in a 1 / 1 SF_6 / Ar mixture above silicon and silicon dioxide surfaces as a function of pressure are shown in Fig. 2. The induction coil power was 200 W and the wafer bias power was 20 W. For these conditions, the electron density above the Si surface was independent of the pressure and the SF_6 / Ar ratio. However, above the SiO_2 surface, the electron density decreased a factor of 2 as the pressure was increased from 5 to 35 mTorr. As with the variation in

induction coil power, this data shows significant differences between the two surface materials, likely due to significant differences in the species evolved from the surface etch of Si vs. SiO_2.

The negative ion density and the scaling with pressure were functions of the surface material. Above the Si surface, the negative ion density increased linearly with pressure, as would be expected with an increase in the concentration of the negative ion molecular precursor XY (for a constant electron density). However, we also observe that the negative ion density is higher in pure SF_6 discharges than in SF_6 / Ar mixtures, despite a lower electron density. Thus the negative ion production is also likely influenced by changes in etch product density or changes in the electron temperature. In the case of a SiO_2 surface, the pressure dependence is quite complicated. Despite a monotonic decrease in the electron density, the negative ion density shows a significant increase when the pressure was increased from 5 to 15 mTorr and a constant density at pressure above 15 mTorr. At lower pressures, the electron density decreased approximately 20 percent while the negative ion density increased a factor of 3 – 4. Such an extremely non linear response must indicate large changes in the negative-ion molecular precursor species, either due to the parent gas and its dissociation products, etch products from the surface, or surface recombination.

Comparison of these measurements in SF_6 with our previous measurements in fluorocarbon containing plasma shows several points. For example, a similar decrease in the electron density with increased pressure was also observed in C_2F_6 and CHF_3 discharges although the decrease in CHF_3 was not as large.[9,10] However, in the case of the fluorocarbon plasmas, the decrease was *independent* of surface material. Consistent with the discussion above, these measurements also suggest that the $C_xH_yF_z$ polymer

layer and not the underlying Si or SiO_2 material dominates the characteristics of the fluorocarbon plasma. In the case of our SF_6 plasma, there is a strong surface dependence that indicates that the surface layer, if present at all, has minimal influence on the bulk plasma properties. The different radical species produced by Si vs. SiO_2 etching of the surface appear to dominate the bulk plasma characteristics. One could even speculate that the major difference involves an O or O_2 containing species since this is the major atomic difference in the surface composition. An increase in the negative ion density with pressure was observed in our previous measurements of the Cl^- negative ion density in Cl_2 and BCl_3 containing inductive discharges.[14,15] In the case of C_2F_6 and CHF_3 discharges above Si surfaces, despite a constant or decreasing electron density, the negative ion density increased only slightly for pressures of 5 to 10 mTorr and was relatively constant above 10 mTorr.[9] This was significantly different from the increasing negative ion density with increased pressure measured in C_4F_8 and indicates that the dominant negative ion formation pathways in the different gases were not the same.[10]

Electron and negative ion densities in pure SF_6 and in a 1 / 1 SF_6 / Ar mixture above silicon and silicon dioxide surfaces as a function of bias electrode power are shown in Fig. 3. The induction coil power was 200 W and the pressure was 10 mTorr. In this case, the electron density was independent of the bias power, even when the bias power was similar to the induction coil power. These results are similar to previous measurements that showed that the electron density was independent of the bias power.[9,10,11] The magnitude of the electron density did depend on the surface material and the SF_6 / Ar ratio. The negative ion density was also independent of the bias power. This point is interesting since it implies that the surface processes that generate species that feed back into the gas phase and influence the electron and negative ion density are

independent of rf bias power. This tends to rule out processes that strongly depend on changes in the ion energy distribution function at the surface.[20,21]

Electron and negative ion densities above silicon and silicon dioxide surfaces as a function of SF_6 / Ar ratio are shown in Fig. 4. For this experiment, the induction coil power was 200 W, pressure was 10 mTorr and the bias power was 20 W. While the slope was surface dependent, in both cases, the electron density increased linearly with increased argon fraction. The negative ion density above SiO_2 was constant for argon fractions of 0 to 0.5 and then decreased linearly to zero for pure argon. Above Si, the decrease in negative ion density was linear. In this figure, we note a small, non-zero negative ion signal that was *not* observed in pure argon in a clean chamber. Thus we attribute the signal to negative ions formed from the sputtering of the uncharacterized material that accumulates on the walls of the chamber during SF_6 etching.

B. Voltage and current measurements

Voltage and current (VI) measurements are beginning to find applications in endpoint detection and tool fault detection.[22,23] Thus voltage and current characteristics of the induction coil and the biased electrode were measured for silicon and fused silica surfaces. The rf voltage and current (zero-to-peak values) for the induction coil, effective coil power loss and the rf biased electrode are reported as functions of induction coil power (Fig. 5), pressure (Fig. 6), bias power (Fig. 7) and SF_6 / Ar ratio (Fig. 8). Induction coil power was measured using a inline power meter between the rf amplifier and the coil matching network. For all measurements reported here, the reflected power was less than 2 W. The net power into the plasma (not shown) is the difference between the input induction coil power and the coil loss due to an effective (measured) coil

resistance that includes the resistance of the coil and wall effects. For a typical coil resistance of 0.4 Ω, approximately 80% of the total input power was deposited in the plasma. In the case of the biased electrode voltage and current, only the values at the fundamental frequency, 13.56 MHz are reported since the values at the second harmonic were approximately 20 percent of the fundamental values and had similar trends. The method to analyze the harmonic content of the waveforms has been previously discussed.[12,13]

A number of trends in the induction coil VI characteristics were observed. While the induction coil voltage and current increased with induction coil power and was independent of rf bias power, consistent with previous measurements[9,10,14], the VI characteristics did not show a large surface dependence. However, the induction coil voltage and current as functions of the pressure and SF_6 / Ar ratio did show a surface dependence. In the case of pressure changes, both the induction coil voltage and current were larger above SiO_2 surfaces than Si surfaces and the difference increased with increased pressure. In the case of changes in the SF_6 / Ar ratio, the induction coil voltage and current were higher above SiO_2 surfaces than above Si surfaces. The difference was largest for gas mixtures that were mostly SF_6. We note that a comparison of the trends in the VI characteristics and the electron density data do not show an obvious correlation. For example, the large changes in the electron density between SiO_2 and Si surfaces at higher induction coil powers was not reflected in the induction coil VI data. However, for high SF_6 concentrations, the electron density above the two surfaces was almost identical but the induction coil VI data shows clear differences. Thus surface dependent changes in the induction coil VI characteristics do not appear to be strongly related to the bulk electron density.

The voltage and current characteristics of the rf biased electrode which holds the Si or SiO_2 wafers were different than the induction coil. The bias voltage measured with a SiO_2 surface was always higher than the value measured with a Si surface. In most cases, the bias voltage was 50 percent higher above a SiO_2 surface than above a Si surface. Such large changes show the potential for using VI measurements as a tool fault monitor or possibly an endpoint detector. Unlike the bias voltage, the bias current did not show an obvious difference between SiO_2 or Si surfaces. We also note that the bias voltage and current were independent of the induction coil power, pressure, and SF_6 / Ar ratio, consistent with previous measurements. [9,10,12,14]

IV. Summary

In conclusion, electron and negative ion densities above silicon and silicon dioxide surfaces were measured in inductively coupled discharges containing SF_6 / Ar gas mixtures. Line integrated electron density was determined using a microwave interferometer and absolute negative ion densities in the center of plasma were inferred using laser photodetachment spectroscopy. For the range of induction powers, pressures, bias power and gas ratios investigated, the electron density peaked at 5×10^{12} cm^{-2} (line-integrated) or approximately 5×10^{11} cm^{-3}. Over this same range the negative ion had a maximum of 2×10^{11} cm^{-3}, and was always less than the electron density.

The use of silicon and silicon dioxide surfaces produced significant differences in the electron and negative ion densities. For most conditions, the electron density above the oxide surface was equal to or slightly higher than the density above a silicon surface. In contrast, the negative ion density above the oxide surface was a factor of 5 to 10 larger than the density above a silicon surface. For our conditions, the negative-ion / electron

density ratio was always less than one. Comparison of these measurements in SF_6 with our previous measurements in fluorocarbon containing plasma shows the importance of the surface material. In the case of the fluorocarbon plasmas, the scaling of the electron and negative ion density tended to be *independent* of surface material, suggesting that the $C_xH_yF_z$ polymer layer and not the underlying Si or SiO_2 material dominate the characteristics of the fluorocarbon plasma. In the case of our SF_6 plasma, there is a strong surface dependence that indicates that the surface layer, if present at all, has minimal influence on the bulk plasma properties. The different radical species produced by Si vs. SiO_2 etching of the surface appear to dominate the bulk plasma characteristics.

In addition to surface dependent changes in the electron and negative ion density, we also measured surface dependent changes in the VI characteristics of the inductive coil and the rf biased electrode. The induction coil VI characteristics showed a marked difference above a SiO_2 surface as opposed to a Si surface as a function of pressure and the SF_6 / Ar ratio but were independent of the inductive coil power and the bias power. We note that a comparison of the trends in the VI characteristics and the electron density data does not show an obvious correlation. The bias voltage measured with a SiO_2 surface was always higher than the value measured with a Si surface. In most cases, the bias voltage was 50 percent higher above a SiO_2 surface than above a Si surface.

V. Acknowledgments

The technical assistance of T. W. Hamilton is gratefully recognized. This work was performed at Sandia National Laboratories and supported by Motorola and Sandia National Laboratories. Sandia is a multiprogram laboratory operated by Sandia

Corporation, a Lockheed Martin Company, for the United States Department of Energy under contract DE-AC04-94AL85000.

Figure Captions

Fig. 1 Line-integrated electron and negative ion density as functions of the induction coil power. The solid symbols are for a 1 / 1 gas mixture of SF_6 / Ar above silicon (!) and silicon oxide (#) surface while the open symbol (') is for pure SF_6 above a silicon surface. The pressure was 10 mTorr with a bias power of 20 W.

Fig. 2 Line-integrated electron and negative ion density as functions of pressure. The solid symbols are for a 1 / 1 gas mixture of SF_6 / Ar above silicon (!) and silicon oxide (#) surface while the open symbol (') is for pure SF_6 above a silicon surface. The induction coil power was 200 W with a bias power of 20 W.

Fig. 3 Line-integrated electron and negative ion density as functions of the substrate bias power. The solid symbols are for a 1 / 1 gas mixture of SF_6 / Ar above silicon (!) and silicon oxide (#) surface while the open symbol (') is for pure SF_6 above a silicon surface. The induction coil power was 200 W at a pressure of 10 mTorr.

Fig. 4 Line-integrated electron and negative ion density as functions of the Ar / SF_6 ratio above silicon (!) and silicon oxide (#) surfaces. The induction coil power was 200 W, pressure was 10 mTorr and the bias power was 20 W.

Fig. 5 Induction coil voltage, current and loss, and biased electrode voltage and current as functions of power into the induction coil. Data for a 1 / 1 SF_6 / Ar ratio above silicon(') and silicon oxide()) surfaces is shown with data for pure SF_6 above a silicon surface(+). The pressure was 10 mTorr with a bias power of 20 W. In the case of the bias voltage and current, only the values at 13.56 MHz are shown. The values at the second harmonic were less than 20 percent of the values at the fundamental.

Fig. 6 Induction coil voltage, current and loss, and biased electrode voltage and current as functions pressure. Data for a 1 / 1 SF_6 / Ar ratio above silicon(') and silicon oxide(○) surfaces is shown with data for pure SF_6 above a silicon surface(+). The induction coil power was 200 W with a bias power of 20 W. In the case of the bias voltage and current, only the values at 13.56 MHz are shown. The values at the second harmonic were less than 20 percent of the values at the fundamental.

Fig. 7 Induction coil voltage, current and loss, and biased electrode voltage and current as functions of the substrate bias power. Data for a 1 / 1 SF_6 / Ar ratio above silicon(') and silicon oxide(○) surfaces is shown with data for pure SF_6 above a silicon surface(+). Induction coil power was 200 W at a pressure of 10 mTorr. In the case of the bias voltage and current, only the values at 13.56 MHz are shown. The values at the second harmonic were less than 20 percent of the values at the fundamental.

Fig. 8 Induction coil voltage, current and loss, and biased electrode voltage and current as functions of the Ar / SF_6 ratio above a silicon(') and silicon oxide(○) surface. Induction coil power was 200 W, pressure was 10 mTorr and the bias power was 20 W. In the case of the bias voltage and current, only the values at 13.56 MHz are shown. The values at the second harmonic were less than 20 percent of the values at the fundamental.

References

[1] R. J. Shul and J. G. Fleming "Bulk Si Micromachining for Integrated Microsystems" in *Handbook of Advanced Plasma Processing Techniques*, R. J. Shul and S. J. Pearton, (Springer-Verlag, Berlin, 2000).

[2] L. G. Christophorou and J. K. Olthoff, J. Phys. Chem. Ref. Data, 29(3), 267 (2000).

[3] T. Kimura and K. Ohe, Appl. Phys. Lett., 79(18), 2874 (2001).

[4] A. Kono, M. Endo, K. Ohata, S. Kishimoto, and T. Goto, J. Appl. Phys., 76(11), 7221 (1994).

[5] L. St-Onge, M. Chaker and J. Margot, J. Vac. Sci. Technol. A, 18(5), 2363 (2000).

[6] C. Riccardi, R. Barni and M. Fontanesi, J. Appl. Phys., 90(8), 3735 (2001).

[7] E. Stamate and K. Ohe, J. Appl. Phys., 84(5), 2450 (1998).

[8] M. Shindo, S. Uchino, R. Ickiki, S. Yoshimura and Y. Kawai, Rev. Sci. Instru., 72(5), 2288 (2001).

[9] G. A. Hebner and P. A. Miller, J. Appl. Phys., 87, 7660 (2000).

[10] G. A. Hebner and I. C. Abraham, J. Appl. Phys., 90(10), 4929 (2001).

[11] G. A. Hebner, M. G. Blain, T. W. Hamilton, C. A. Nichols and R. L. Jarecki, J. Vac. Sci. Technol. A, 17, 3172 (1999).

[12] P. A. Miller, G. A. Hebner, K. E. Greenberg, P. D. Pochan and B. P. Aragon, J. Resch. Natl. Int. Standard. Technol 100, 427 (1995).

[13] P. J. Hargis Jr., K. E. Greenberg, P. A. Miller, J. B. Gerardo, J. R. Torczynski, M. E. Riley, G. A. Hebner, J. R. Roberts, J. K. Olthoff, J. R. Whetstone, R. J. Van Brunt, M. A. Sobolewski, H. M. Anderson, M. P. Splichal, J. L. Mock, P. Bletzinger, A. Garscadden, R. A. Gottscho, G. Selwyn, M. Dalvie, J. E. Heidenreich, J. W. Butterbaugh, M. L. Brake, M. L. Passow, J. Pender, A. Lujan, M. E. Elta, D. B. Graves, H. H. Sawin, M. J. Kushner, J. T. Verdeyen, R. Horwath and T. R. Turner, Rev. Sci. Inst. 65, 140 (1994).

[14] G. A. Hebner, J. Vac. Sci. Technol. A. 14(4), 2158 (1996).

[15] C. B. Fleddermann and G. A. Hebner, J. Vac. Sci. Technol. A, 15(4), 1955 (1997).

[16] A. Mandl, Phys. Rev. A, 3(1), 251 (1971).

[17] S. Vacquie, A. Gleizes and M. Sabsabi, Phys. Rev. A, 35(4), 1615 (1987).

[18] K. E. Greenberg and G. A. Hebner, J. Appl. Phys., 73(12) 8126 (1993)

[19] G. A. Hebner, J. Appl. Phys., 89(2) 900 (2001).

[20] M. G. Blain, J. E. Stevens and J. R. Woodworth, Appl. Phys. Lett., 75(#25), 3923 (1999).

[21] C. A. Nichols, J. R. Woodworth, and T. W. Hamilton, J. Vac. Sci. Technol. A 16(#6), 3389 (1998).

[22] M. A. Sobolewski and K. L. Steffens, J. Vac. Sci. Technol. A., 17(#6), 3281 (1999).

[23] B. Kim and C. Lee, J. Vac. Sci. Technol. A, 18(1), 58 (2000).

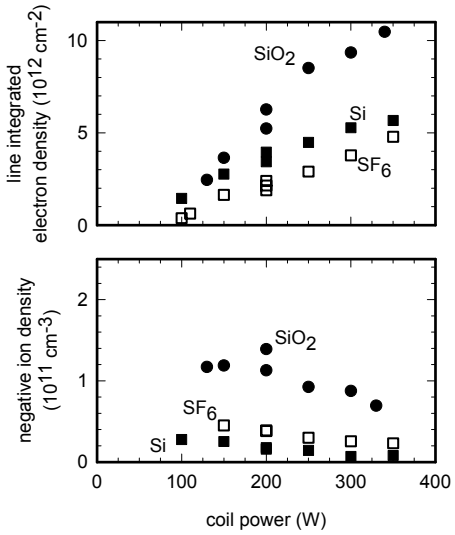
line integrated
electron density (10^{12} cm^{-2})
10
5
0
SiO_2
Si
SF_6
negative ion density
(10^{11} cm^{-3})
2
1
0
SiO_2
SF_6
Si
0
100
200
300
400
coil power (W)

Fig. 1
Hebner

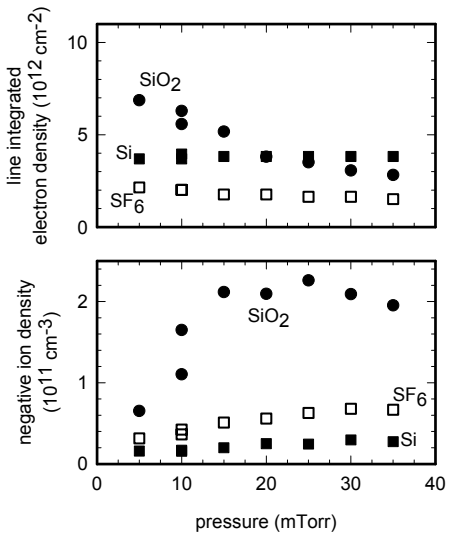
line integrated
electron density (10^{12} cm^{-2})
10
5
0
SiO_2
Si
SF_6
negative ion density
(10^{11} cm^{-3})
2
1
0
SiO_2
SF_6
Si
0
10
20
30
40
pressure (mTorr)

Fig. 2
Hebner

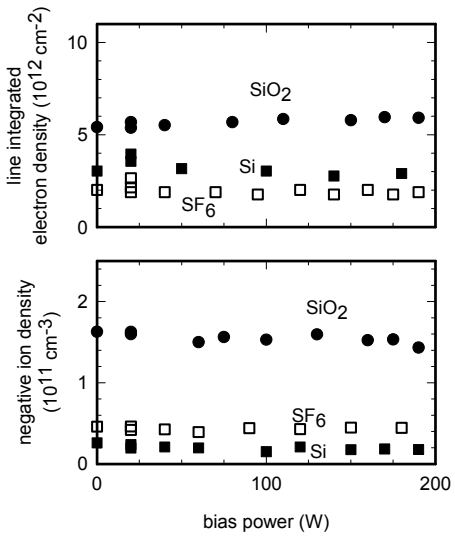
line integrated
electron density (10^{12} cm^{-2})
10
5
0
SiO_2
Si
SF_6
negative ion density
(10^{11} cm^{-3})
2
1
0
SiO_2
SF_6
Si
0
100
200
bias power (W)

Fig. 3
Hebner

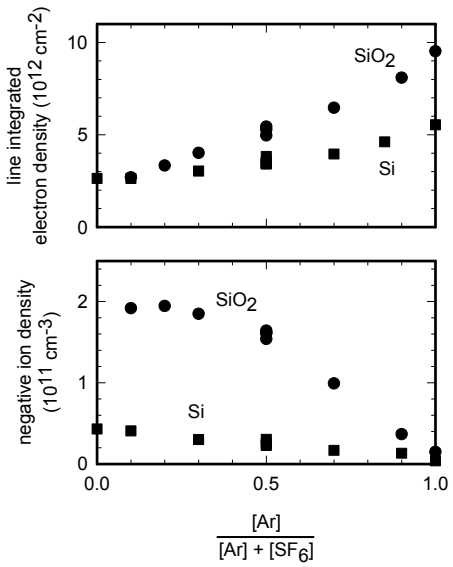
line integrated
electron density (10^{12} cm^{-2})
10
5
0
SiO2
Si
negative ion density
(10^{11} cm^{-3})
2
1
0
SiO2
Si
0.0
0.5
1.0
[Ar]
[Ar] + [SF6]

Fig. 4
Hebner

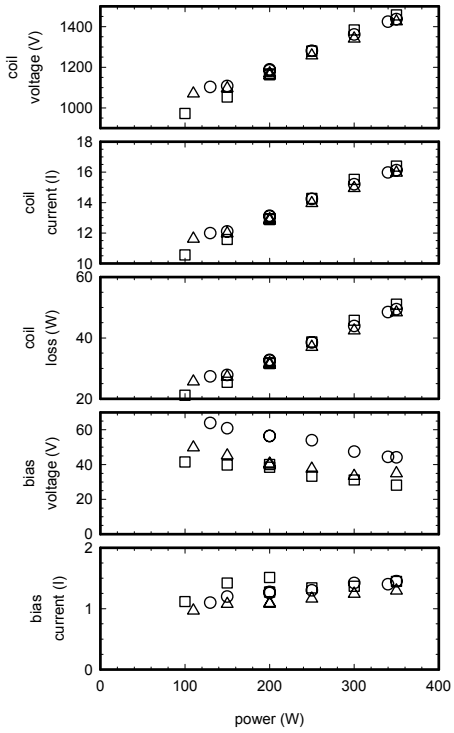
coil voltage (V)
1400
1200
1000
coil current (I)
18
16
14
12
10
coil loss (W)
60
40
20
bias voltage (V)
60
40
20
0
bias current (I)
2
1
0
0
100
200
300
400
power (W)

Fig. 5
Hebner

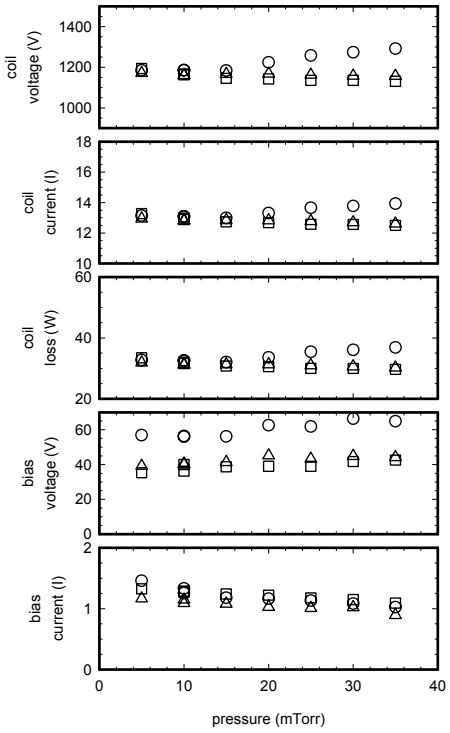
coil voltage (V)
1400
1200
1000
coil current (I)
18
16
14
12
10
coil loss (W)
60
40
20
bias voltage (V)
60
40
20
0
bias current (I)
2
1
0
0
10
20
30
40
pressure (mTorr)

Fig. 6
Hebner

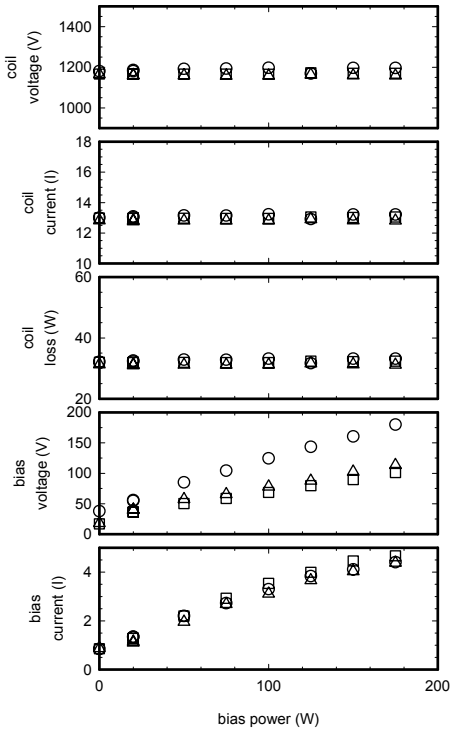
coil voltage (V)
1400
1200
1000
coil current (I)
18
16
14
12
10
coil loss (W)
60
40
20
bias voltage (V)
200
150
100
50
0
bias current (I)
4
2
0
0
100
200
bias power (W)

Fig. 7
Hebner

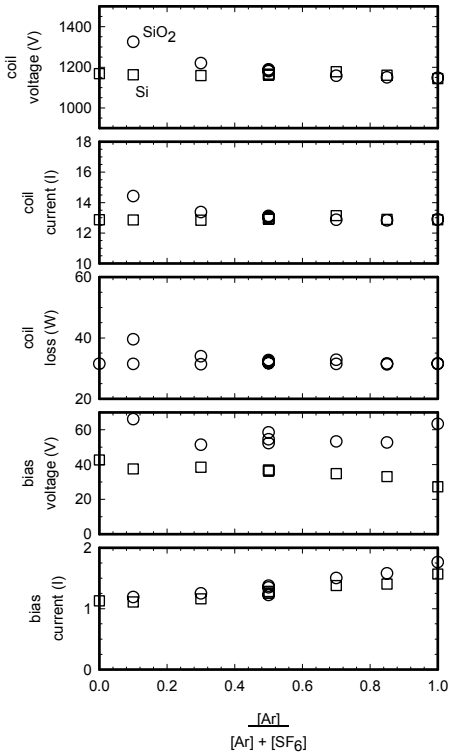
coil voltage (V)
1400
1200
1000
SiO2
Si
coil current (I)
18
16
14
12
10
coil loss (W)
60
40
20
bias voltage (V)
60
40
20
0
bias current (I)
2
1
0
0.0
0.2
0.4
0.6
0.8
1.0
[Ar]
[Ar] + [SF6]

Fig. 8
Hebner

Appendix 4

Ions in holes : an experimental study of ion distributions inside surface features on rf-biased wafers in plasma etching discharges

I. Introduction

In this chapter we present an experimental study of ion fluxes, energy distributions and angular distributions inside surface features on rf-biased wafers in high-density, inductively-driven discharges in argon. Specifically, we present data on ion distributions at the bottom of 100-micron-square, 400-micron-deep "holes" in the wafer.

Inductively-coupled plasma discharge reactors are used for the etching of many devices, such as integrated circuits, microelectromechanical systems (MEMS), and photonic circuits. In inductively coupled discharges, an rf-coil couples energy through a dielectric window to excite a low pressure plasma. The wafer to be etched is placed on a chuck in direct contact with the plasma and is bombarded by plasma ions and neutrals. Normally an rf bias voltage is also applied to the chuck and wafer, influencing the energy of the ions striking the wafer. An advantage of these discharges is that the induction coil controls the plasma density and temperature as well as the flux of ions to the wafer, while the energy of the ions striking the wafer can be controlled independently, by adjusting the wafer bias. Several authors[1-5] have recently published extended descriptions of the theory of ion energy distributions in these discharges. In this paper, we report investigations of the effects of sub-millimeter-sized wafer structures on the ion energy and angular distributions.

Experiments coupled to models have greatly improved our understanding of the bulk discharges in these reactors.[6-8] A number of authors have reported measurements of ion energy distributions at grounded electrodes in plasma etching discharges[9-17]. Some authors have reported ion energy distributions at an rf-biased wafer in capacitively-driven discharges.[18-22] Comparatively few authors have reported data on ion energy distributions at the rf-biased electrodes in inductively driven discharges.[23 24 25] Mizutani et. al.[26] have recently reported ion energy and angular distribution measurements in a low-density plasma with a collisional sheath. Edelberg et al.[27] have reported measurements of IEDs in an inductively driven discharge operating in the "low frequency limit" as described by Metze et. al. [28] in which the rf period is much longer than the ion transit time through the sheath. The authors of this work have recently reported ion energy and angular distributions on rf biased wafers in inductively driven discharges at a fixed bias frequency [29]and ion energy distributions as a function of bias frequency.[30] In the current work, we extend our measurements down inside small holes on wafers in etching discharges. We focus on the effects of the holes on the ion energy and angular distributions. This work provides information about sheath behavior near surface structures and demonstrates effects that are important for MEMS fabrication.

II. Apparatus.

Discharge Cell

Our experiments were carried out using pure argon discharges in a Gaseous Electronics Conference Reference Cell (GEC Ref Cell)[31] which had been modified to produce inductively driven discharges.[32] Figure 1 shows a schematic of our GEC Ref Cell. A

five-turn spiral rf-induction coil above the fused silica window on top of the cell was driven at a frequency of 13.56 MHz to excite the plasma. A 15-cm diameter wafer chuck at the bottom of the discharge was almost entirely covered with an undoped single-crystal Si wafer or wafer sections. The chuck was also driven at 13.56 MHz and phase-locked to the induction coil. A double Langmuir probe was used to measure the plasma density and electron temperature.[33-35] We did not measure the DC component of the plasma potential due to the difficulty of making accurate single Langmuir probe measurements in these poorly grounded plasmas. The rf component of the plasma potential was measured with a cylindrical capacitive voltage probe inside a glass pipe which was immersed in the plasma. The rf component of the voltage on the wafer chuck was measured with a flat, ~1-cm diameter, Kapton-encapsulated capacitive voltage probe held against the bottom of the chuck.[36, 37] In addition to measuring the rf component of the plasma and wafer potentials, we used the two rf voltage monitors to measure and adjust the phase between these two potentials. We adjusted the coil and chuck power supplies so that the 13.56-MHz component of the plasma and chuck potentials were in phase.

Under most conditions, the plasma was well contained in a ~10-cm diameter region between the fused silica window and the wafer. The window-to-wafer distance was 3.5 cm. Therefore, the stainless steel window holder appeared to be the most important grounded surface in contact with the plasma. The stainless steel vacuum chamber walls at a 25-cm radius appeared much less important as a ground surface.

A copper Faraday shield[38] was placed between the rf induction coil and the quartz entrance window to suppress capacitive coupling between the rf coil and the plasma. An

aluminum cylinder (11 cm outer diameter, 12 cm tall, 0.5 cm thick) was also slipped inside the recessed window-holder to reduce resistive losses due to induced currents in the surrounding stainless steel[32]. A 0.25 cm-thick Teflon insulator was placed between the Faraday shield and the rf coil. The Faraday shield typically reduced rf potential fluctuations in the plasma potential caused by the inductive coil to less than two volts peak-to-peak. Plasma potential fluctuations caused by the chuck bias however, could be considerably larger.

It was necessary to cover most of the chuck surface with Si to prevent metal ions from sputtering off the stainless steel chuck and coating the fused silica rf coupling window when the chuck was biased. Figure 2 shows a top view of our chuck with the wafer components on it. In the center of the figure is a 4.6-mm square, 300–micron-thick, Si wafer with a 2.9-mm square hole in it. The center of this 2.9-mm square hole functioned as our "flat wafer" measurement for these experiments. Previous work[39] suggests that the ion energy and angular distributions we measured in the center of a hole which was 2.9-mm square and only 300-microns deep should be very close to the distributions on a flat surface.

For the 100-micron-hole experiments, the 4.6-mm square Si wafer with one large hole in it was replaced by a wafer of similar size but 400-um thickness having an array of 100-um square holes in it (fig. 3). The 4.6-mm square wafers were attached to the stainless wafer chuck with a small amount of conductive epoxy. A differentially-pumped pinhole at the bottom of the 100-micron square holes led to a separate vacuum system containing our gridded ion analyzer. The laser-drilled pinholes were 6 microns in diameter and

were in a nickel foil estimated by the manufacturer to be between 2 and 3 microns thick.[40] We varied the position of the pinhole relative to the walls and holes by gluing nominally identical walls and holes down at different distances from "identical" pinholes. The pinholes used in these experiments were produced in two runs by the manufacturer, with the pinholes used for the measurements on a flat surface having a diameter of ~5.5 microns and the pinholes used for the measurements in the holes having a diameter of ~6.5 microns. All the pinholes in each run appeared to have identical diameters to our experimental uncertainty of $\pm$ 10%.

Gridded Ion Analyzer

Figure 4 shows a schematic of our gridded ion energy and angle analyzer that has been described in detail previously.[41] The analyzer contains three screen grids and a series of round current collection electrodes. The 0.48-cm diameter stainless steel collection electrodes were stacked in a hexagonal close-packed array as shown in Fig. 5. The three grids and the surface of the bundle of electrodes formed sections of nested concentric spheres, all of which were centered on the pinhole. Hence, the surfaces of all the electrodes were on a spherical surface located 2.3 cm from the pinhole. The first and third grids were a woven stainless steel mesh[42] with ~20 wires/cm and an open area of 92%. The second grid was also woven of stainless steel mesh but had ~40 lines/cm and an open area of 81%. The first grid (nearest the pinhole) was held at local ground (the wall of the rf-biased chuck) to provide a field-free drift region. The voltage on the second grid was varied from 0 to + 60 Volts to map out the ion energy distribution. When the second grid voltage was set at V_0 only ions with energies greater than V_0

would pass through the grid and reach the electrodes. Thus, the derivative of the signal on the collection electrodes as a function of the voltage on the middle grid yielded the ion energy distribution. [39]

The third grid was held at a negative potential (typically minus 40 volts) to prevent electrons from the discharge from reaching the collection electrodes and to suppress secondary electron emission from the electrodes. Because the grids and collection electrodes are sections of spheres centered on the pinhole, ion trajectories will not be affected by any external electric fields as the ions travel from the pinhole to the electrodes. As a result, we can measure the ion angular distributions at the pinhole by comparing the current on the various electrodes. Based on previous work, we expect the sensitivity of this instrument to be independent of ion energy. The energy resolution of this detector (stated as $\Delta E/E$) is about 5%.[43] Thus for 20 eV ions, we expect the detector resolution to be about 1 eV.

A point of great experimental importance is that the entire gridded analyzer was floated at the rf potential of the wafer chuck. In order to get the control voltages and collector currents into and out of the analyzer, we passed the signals through rf low-pass filters[44] as shown in Fig. 6. The rf low-pass filters passed DC currents with almost no attenuation, but attenuated signals at 13.56 MHz or higher by at least 50 dB. The filters also had high input impedances at 13.56 MHz in order to avoid shorting out the chuck. After extraction from the rf biased area, the collector currents were passed through a low current switching system to a pico-ammeter. The switching system, the pico-ammeter,

and the power supplies for the grid voltages were all controlled by a computer operating on “LabView” software.

III. Results

Table I lists plasma densities and electron densities measured with our double Langmuir probe for the Ar discharges in these experiments. Table I also lists our estimates of the Debye lengths and sheath sizes (against a flat wafer) for these discharges. Sheath widths are theoretical estimates taken from other work in these discharges[45] that define the sheath edge as the location where time-averaged relative charge density is equal to 1% or $(n_i–n_e)/ n_e = 0.01$. This definition typically produces sheath widths of 6 to 9 Debye lengths. Note that in some previous work,[30] we defined the sheath edge as the point where the time-averaged potential has relaxed from its value at the wall to within 1/e of its value in the bulk plasma. This previous definition typically produced sheath widths of ~3 Debye lengths.

Figures 7 and 8 show plots of ion flux to the bottom of our 100-micron-square, 400-micron deep holes in Si wafers. These figures show transmission as a function of distance from the wall of the hole with and without rf bias on the wafer. Data is shown for several induction powers, or equivalently, for several plasma sheath widths. To obtain values of transmission, we compared ion fluxes at the bottom of our 100-micron holes to ion fluxes at a flat area on the chuck in nominally identical discharges. The ion fluxes to flat areas varied from 10 to 25 mA/cm^2. The 6-micron diameter “sampling aperture” moves from the center of the square hole (50 microns from wall) to a location

grazing the center of one straight section of the wall (4 microns from wall). Several trends are apparent from these figures. First, all the transmissions on the biased wafer are higher than the corresponding transmissions on the wafer with no bias. Second, while there is some variation, the transmissions are relatively constant across the bottom of the hole. Third, as the induction power increases and the sheath width shrinks, becoming comparable to the hole size, the transmission decreases.

Figure 9 shows transmitted ion flux to the center of our 100-micron-square holes as a function of average ion energy and sheath size. As seen in the previous two figures, transmission decreases as the sheath thickness shrinks. We also note that transmission increases as the average ion energy increases. Average ion energy was changed either by varying the pressure in the discharge, or by varying the rf bias power.

Figures 10 and 11 show ion energy distributions recorded at the bottom of the 100-micron holes and compare them to ion energy distributions recorded on a flat electrode in a nominally identical discharge**.** In both cases the width of the IED's between peaks on the flat surface is almost equal to the peak-to-peak voltage difference between the wafer and plasma, indicating that we were in the low frequency limit.[30] The IED's in the hole are consistently narrower than the IEDs on the flat surface and the width of the IED does not appear to vary as we move from the center of the hole to the wall.

Figures 12 – 14 show ion angular distributions in the bottom of our 100-um square, 400-um deep holes. Figure 12 shows IADs for 23 mT, 100 W discharges (~250 um-sheaths) with ~28 Vpp rf bias between the chuck and the plasma. Figures 13 and 14 shown IADs

for 23 mT Ar discharges with 250 W of induction coil power (~170 um sheaths) for cases without and with rf bias on the wafer. Figure 15 shows a "side view" plot of some of the data in Fig. 14. It is clear from Fig. 15 that the ions reaching the center of the hole bottom are well collimated, in a beam that is normal to the wafer surface. The ions reaching the edge of the hole bottom however, are peaked at ~12 degrees off normal and have a broad angular distribution.

IV. Discussion

Many of the effects we see in the previous section can be explained in terms of the curvature of equipotential lines and an increase in sheath size near the holes. Figure 16 shows a schematic of electric equipotential lines around two holes with different sheath sizes. In Fig. 16-A the sheath thickness is comparable to the 100-micron square hole. Hence, the equipotential lines bow into the hole. The curvature in the field lines will cause ions falling through the sheath to be deflected away from the center of the hole, lowering the transmission of ions to the bottom of the hole. Higher energy ions will have a larger turning radius, and hence a larger transmission. In Fig 16-B, the sheath thickness is much larger than the hole size. In this case, the equipotential lines are almost straight over the top of the hole, so that ions are only slightly deflected, leading to a higher transmission than in Fig 16-A.

In both cases shown in Fig. 16, we expect the sheath over the hole to be wider than the sheath over a flat surface. As a result, the ions will take a longer time and hence larger fraction of the rf cycle to traverse the sheath in the hole than over the flat surface. Thus, ions detected at the bottom of the hole will have seen more of a time-averaged rf

potential, leading to a narrower IED than the ions detected on the flat surface where the sheath is narrower.

We would have expected to see the ion angular distributions move smoothly off axis as the sampling point in the bottom of the 100-micron hole moved from the center to the edge of the hole because of the ion deflections caused by the bowing of the equipotentials. We were surprised that we did not see the ion angular distributions move off axis until the sampling point was virtually touching the edge of the wall. Most of the movement off axis, however, may have simply been lost in the relatively crude angular resolution of our detector (each pin had an angular diameter seen from the pinhole of 12 degrees). We are constructing a detector with roughly twice the resolution for future experiments. It is important to note that in most cases, as the sampling aperture became very close to the wall, the entire angular distribution shifted towards the wall. If the IAD at this location were dominated by ions that had scattered off the wall, we would expect the angular distribution to shift away from the wall, not toward it. We conclude that for most cases, we saw no evidence in the angular distributions of any flux of ions reaching the bottom of the hole after reflecting off the sides of the hole. The one exception to this rule is seen in the data close to the wall in Fig. 15. This data is for a relatively high pressure, (20 mTorr) with a rf bias on the wafer. The three lower left-most pins (arrowed) record ions that were traveling away from the wall. These pins account for ~10% of the total ion flux to the bottom of the hole and may represent ions that were scattered off the wall. It is also possible that these ions collided with other ions or neutrals inside the hole or that they were perturbed by local electric fields caused by space charge build-up on the walls of the hole.

V. Summary

We have demonstrated ion distribution measurements inside surface features on rf-biased wafers in plasma etching discharges. Transmission of ions to the bottom of our 100-micron-square, 400-micron-deep holes varied from 4% to 30%of the flux to the uniform flat part of the wafer. Transmission increased with ion energy and decreased as sheath size shrank to a size comparable to hole size. Ion energy distributions at the bottom of the holes were narrower than IEDs on a flat surface, because ions took longer to traverse the broader sheaths over the holes. Over most of the hole area, ion flux at the bottom of the hole was normal to the wafer surface, within the limits of the angular resolution of our detector. Very close to the wall (~3-6 microns), however, the ion flux turned ~12 degrees toward the wall and the angular spread of the beam grew significantly. Scattering of ions off the sidewalls of the hole appears to be at most, only a minor source of the ion flux at the bottom of the hole.

Finally, we have demonstrated that we have adequate sensitivity to measure details of ion trajectories inside small surface features on rf-biased wafers during etching.

The authors acknowledge the contributions of P. A. Miller, R. J. Shul, I. C. Abraham, B. P. Aragon, T. W. Hamilton and C. G. Willison to this work.

Table I: Measured electron densities and temperatures and estimates of Debye lengths and sheath thickness. The sheath edge is defined[45] as the location where time-averaged relative charge density is equal to 1% or $(n_i – n_e)/ n_e = 0.01$

Pressure (milliTorr)	Induction Coil Power (Watts)	Electron Temperature (eV)	Electron density ($10^{11}/cm^3$)	Debye length (μm)	Approx. sheath thickness (μm)
5	250	3.7	1.3	38	287
23	100	2.5	1.25	32	248
23	250	2.6	3.7	19	173
23	380	2.7	6.0	16	117

0

Figure Captions:

Figure 1: Schematic of inductively-coupled GEC Ref. Cell with rf biased wafer chuck. The ion analyzer looks through a 6-micron pinhole on the chuck to view the ions impacting the wafer.

Figure 2: Top view of the rf-biased chuck with Si wafers on it. The small square piece in the center contained either the 2.9-mm square hole or the 100-micron square holes. The four silicon "petals" around the square were placed there to prevent sputtering of the stainless steel wafer chuck.

Figure 3: Photomicrograph of an array of 100-micron-square, 400-micron deep holes on our rf biased chuck. Our 6-micron diameter sampling aperture is visible (arrow) near the wall of one of the square holes. The silicon square containing the array was glued to a removable part of our wafer chuck with conductive epoxy.

Figure 4: Schematic of the three-screen gridded energy analyzer. The grids and the array of collection electrodes were formed into sections of nested hemispheres, all centered on the pinhole. This "nested hemisphere" format allowed us to measure ion angular distributions as well as ion energy distributions.

Figure 5: Front view of the collector elements in our ion analyzer. Each pin in the detector subtended a full angle of about 12 degrees as seen from the pinhole.

Figure 6: Electrical schematic for ion analyzer. All signals in and out of the analyzer were passed through rf low pass filters which attenuated the 13.56 MHz chuck bias by ~50 dB or more. This figure shows only one collector pin for simplicity. In reality there were 17 active collector pins and a total of 20 rf low-pass filters.

Figure 7: Transmission of ions to bottom of 100-micron square, 400-micron-deep hole in Si wafer versus location in the hole for several inductive drive powers in 23 mTorr Ar discharges. There was no rf bias on the chuck for these measurements.

Figure 8: Transmission of ions to bottom of 100-micron square, 400-micron-deep hole in Si wafer versus location in the hole for several inductive drive powers in 23 mTorr Ar discharges. The peak-to-peak rf bias between the wafer and plasma varied from 17 to 25 Volts for this data.

Figure 9: Transmission of ions to center of bottom of 100-micron square holes versus average ion energy and sheath size. Transmission increases with increasing energy, but decreases as sheath size becomes comparable to the 100-um square hole.

Figure 10: Comparison of ion energy distributions at bottom of 100-micron square hole and on flat surface. All this data was taken in 23 mTorr Ar discharges with 250 W inductive drive and an rf peak-to-peak voltage of 21 V between the wafer and the plasma. The ion energy distributions inside the hole are offset below zero for clarity.

Figure 11: Comparison of ion energy distributions at bottom of 100-micron square hole and on flat surface. All this data was taken in 5 mTorr Ar discharges with 250 W inductive drive and an rf peak-to-peak voltage of 24 V between the wafer and the plasma. The ion energy distributions inside the hole are offset below zero for clarity.

Figure 12: Ion angular distributions at bottom of 100-micron-square, 400-micron-deep hole versus distance from wall of hole. 23 mTorr Ar discharge with 100 W inductive power and no rf bias on chuck. The white rectangle shows schematically the direction to the nearest wall. The smallest to largest rings are 6.4, 12.8, and 19.2 degrees off the axis of the pinhole, respectively.

Figure 13: Ion angular distributions at bottom of 100-micron square, 400-micron deep hole versus distance from wall of hole. 23 mTorr Ar discharge with 250 Watts inductive drive and no rf bias on chuck. The white rectangle shows schematically the direction to the nearest wall. The smallest to largest rings are 6.4, 12.8, and 19.2 degrees off the axis of the pinhole, respectively.

Figure 14: Ion angular distributions at bottom of 100-micron square, 400-micron deep hole versus distance from wall of hole. 23 mTorr Ar discharge with 250 Watts inductive drive and 21 Volts peak-to-peak rf bias between wafer and plasma. The white rectangle shows schematically the direction to the nearest wall. The smallest to largest rings are 6.4, 12.8, and 19.2 degrees off the axis of the pinhole, respectively.

Figure 15: "Side view" of ion angular distribution data demonstrating that ion beam is on axis and well collimated in center of hole (A), but is ~12 degrees off axis and has a broad angular distribution when the sampling aperture is centered 4 microns from the wall of the hole (B). This data was taken in 23 mTorr Ar discharges with 250 W of inductive drive and 21 V of rf bias between plasma and chuck. In (B) the arrows point to the analyzer pins that have detected ions aimed away from the wall, which may have been scattered off the wall.

Figure 16: Schematics of equipotential lines bowing near 100-micron-square holes A) for case when sheath size is comparable to 100-microns and B) for case when sheath is much larger than 100-microns. Smaller sheaths lead to more strongly curved equipotential lines. Strongly curved equipotentials lead to more deflection of ions, lowering transmission.

Fig 1: J. R. Woodworth et. al. JAP

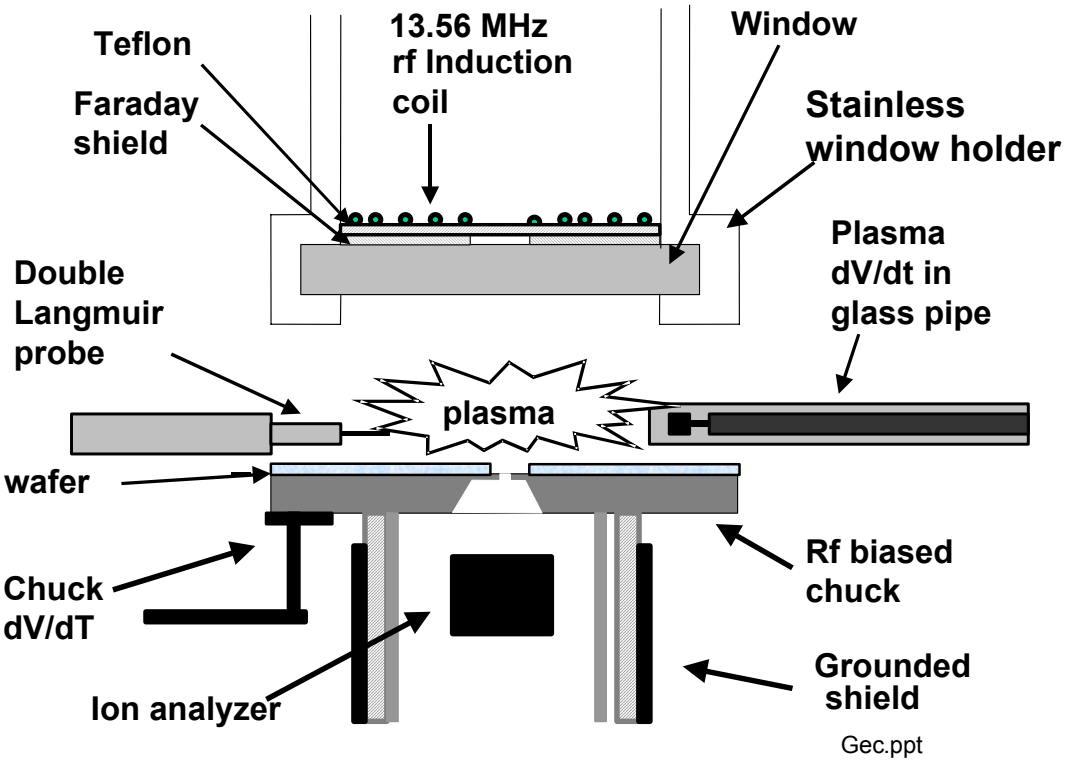

Fig. 2, J. R. Woodworth et. al. JAP

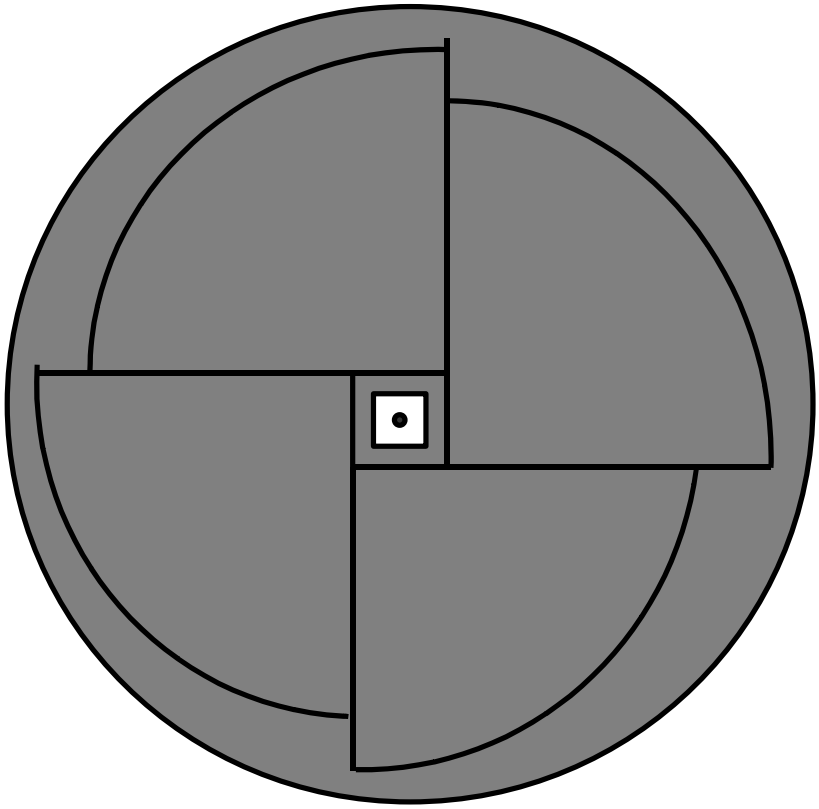

J. R. Woodworth et. al. JAP Fig. 3

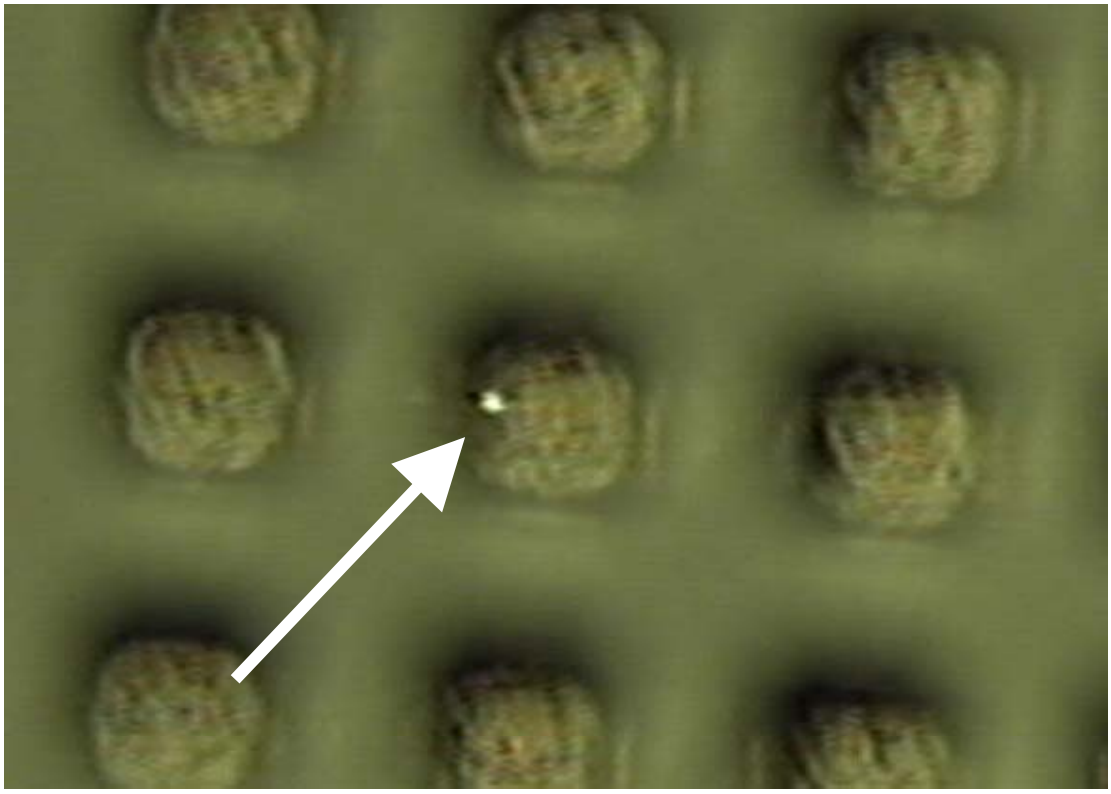

Figure 4; J. R. Woodworth et. al. JAP

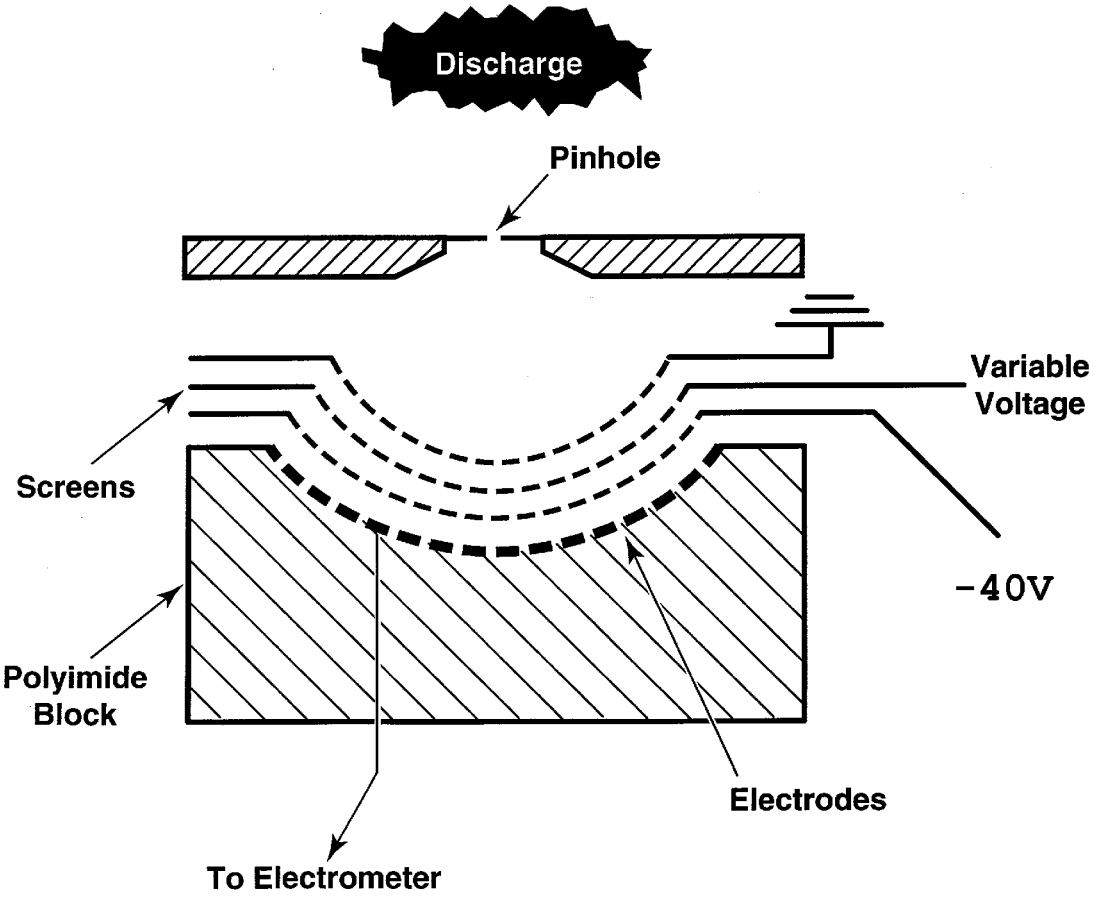

Fig. 5. J. R. Woodworth et. al. JAP

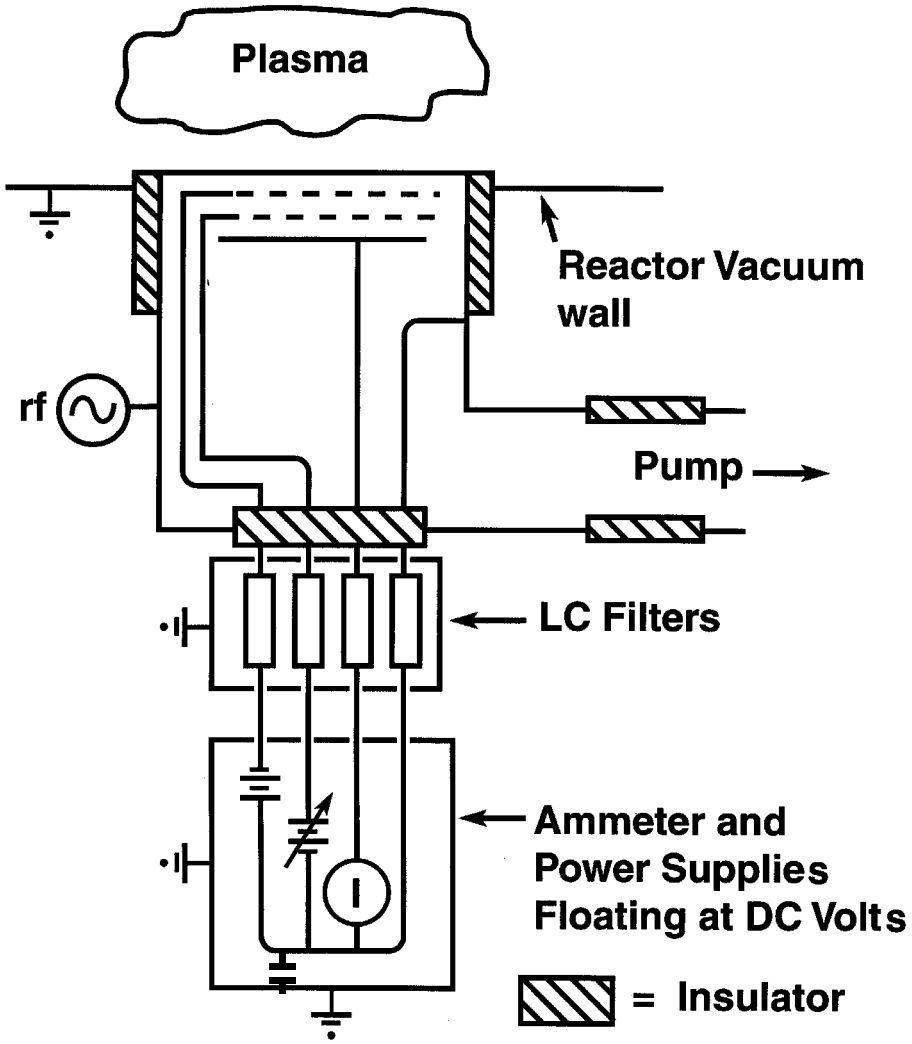

Figure 6, J. R. Woodworth et. al. JAP

Fig. 7, J. R. Woodworth et. al. JAP

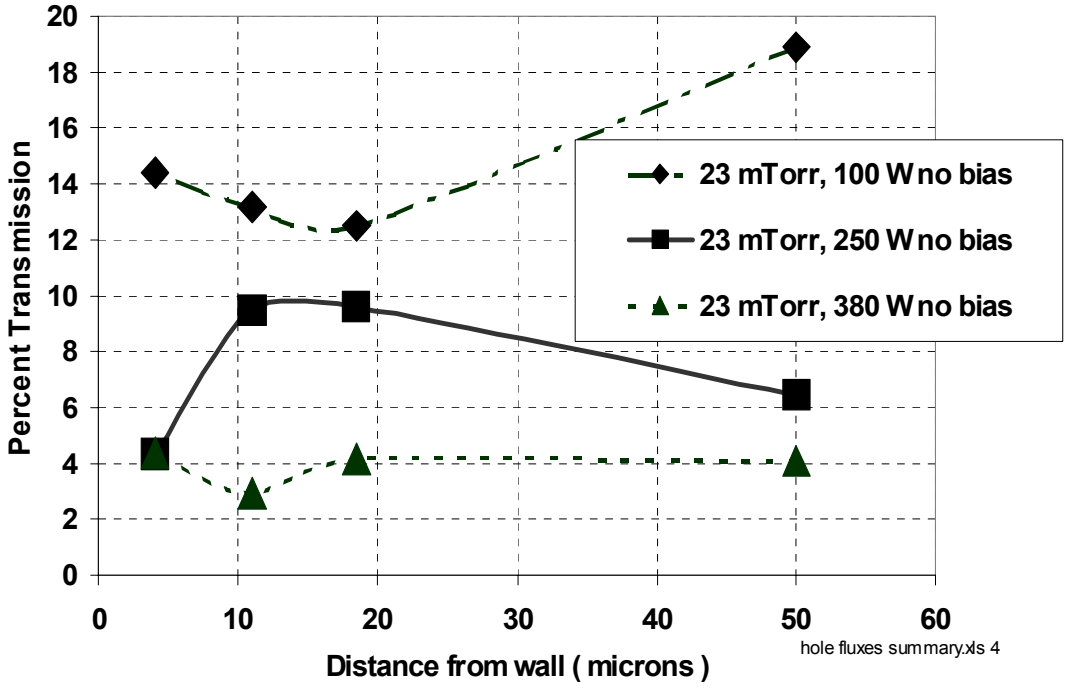

Fig. 8, J. R. Woodworth et. al. JAP

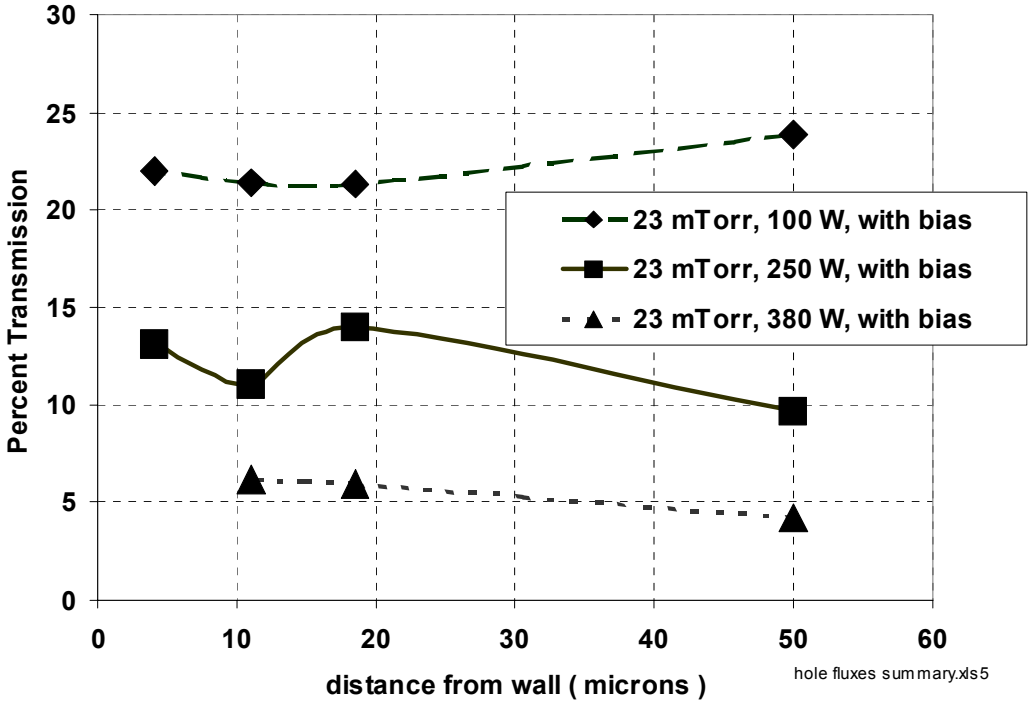

Fig. 9, J. R. Woodworth et. al. JAP

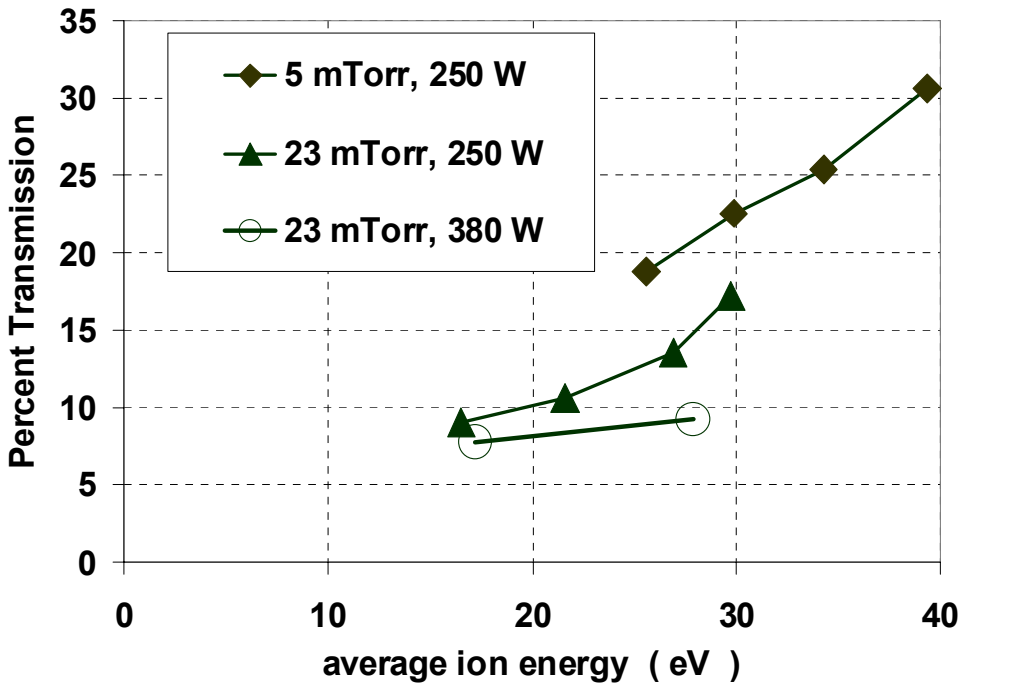

Figure 10, J. R. Woodworth et. al. JAP

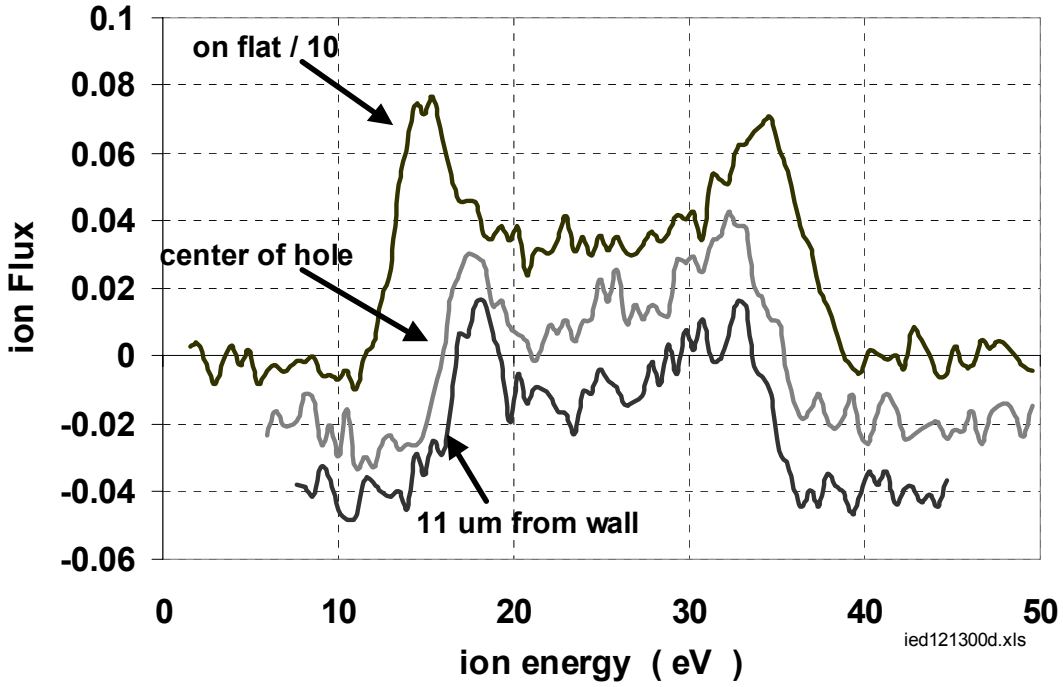

Figure 11, J. R. Woodworth et. al. JAP

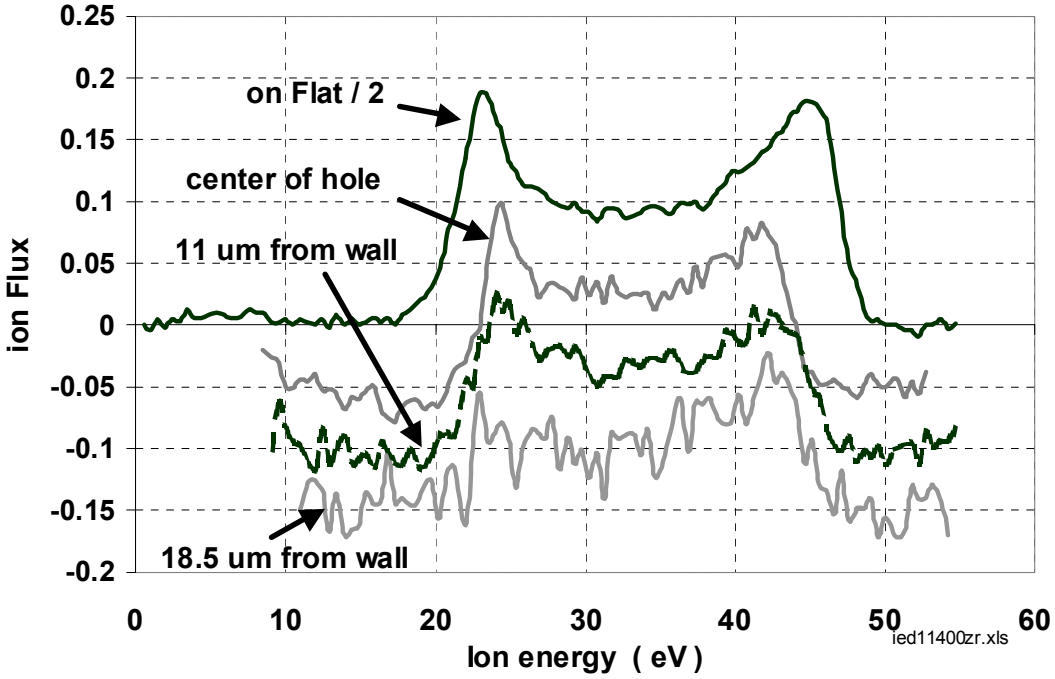

Fig. 12, J. R. Woodworth et. al. JAP

iad121400b.ppt

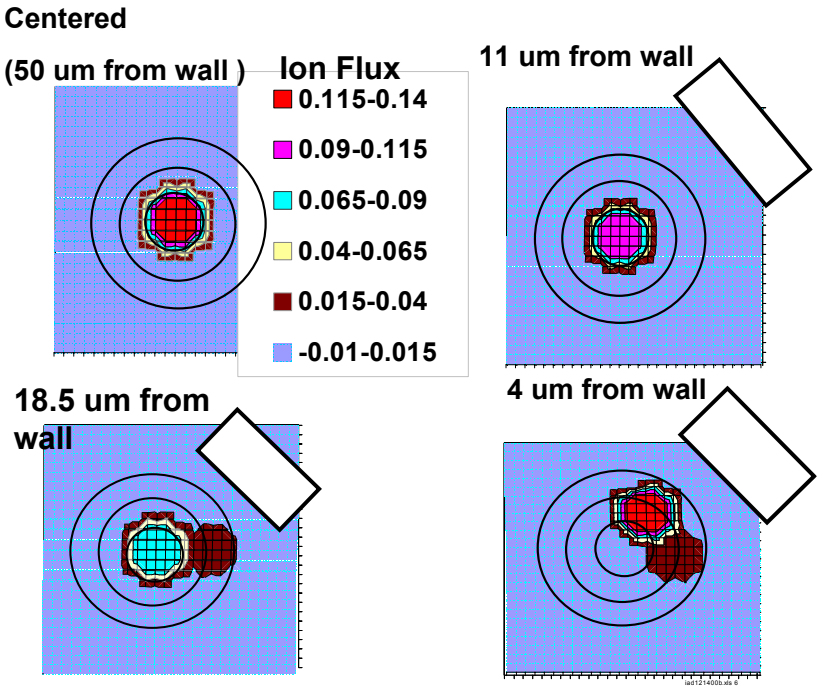

Fig. 13, J. R. Woodworth et. al. JAP

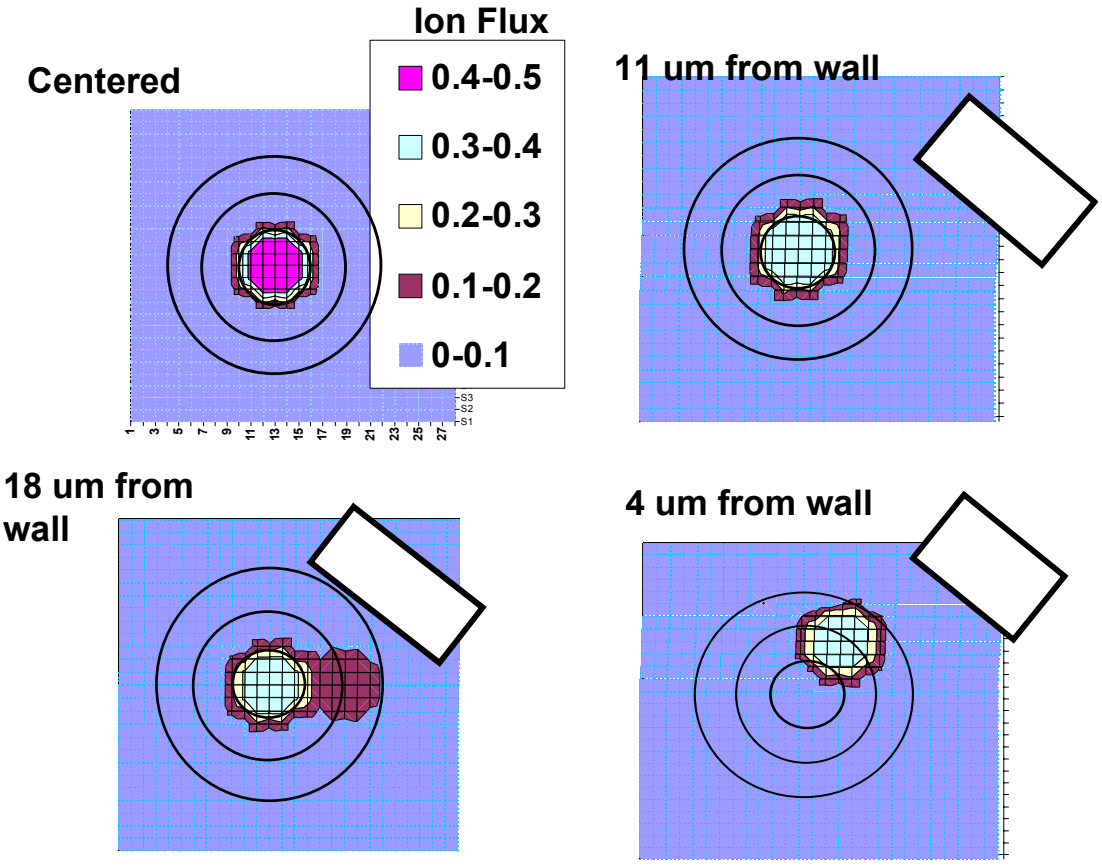

Fig. 14, J. R. Woodworth et. al. JAP

Hole 23 micron
biased data.ppt

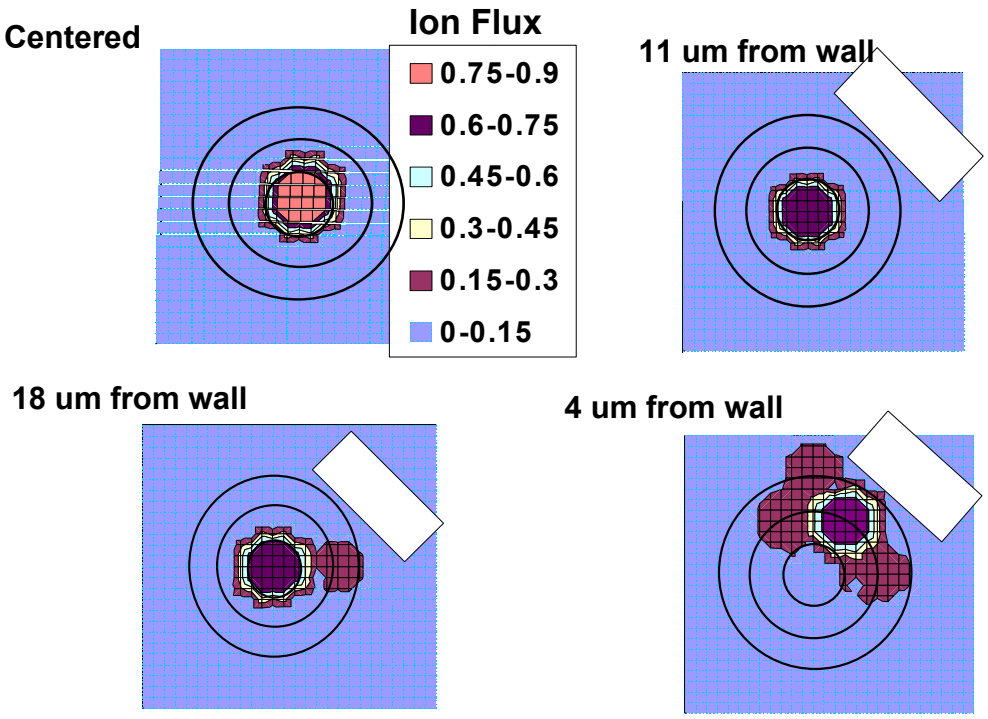

Figure 15 J. R. Woodworth et. al. JAP
23 mTorr, 250 W with rf bias

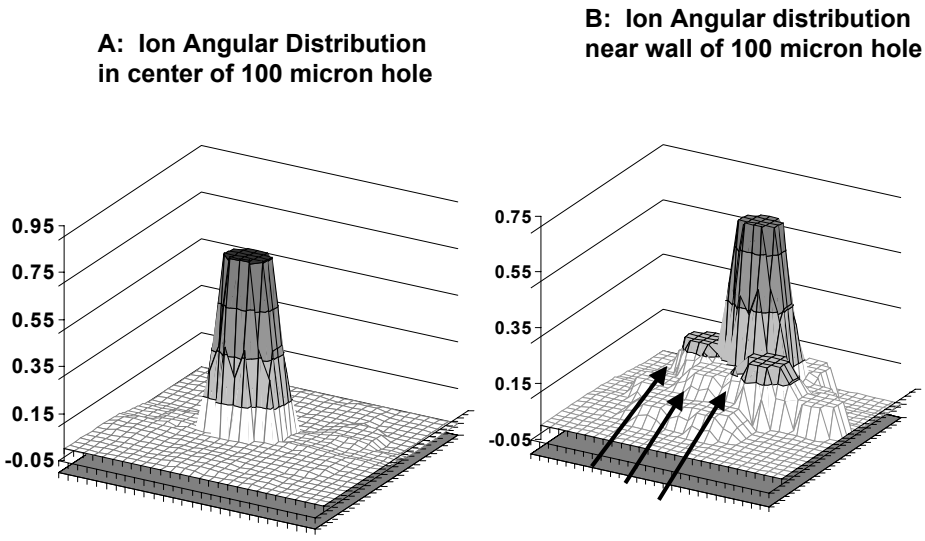

Fig 16 J. R. Woodworth et. al. JAP

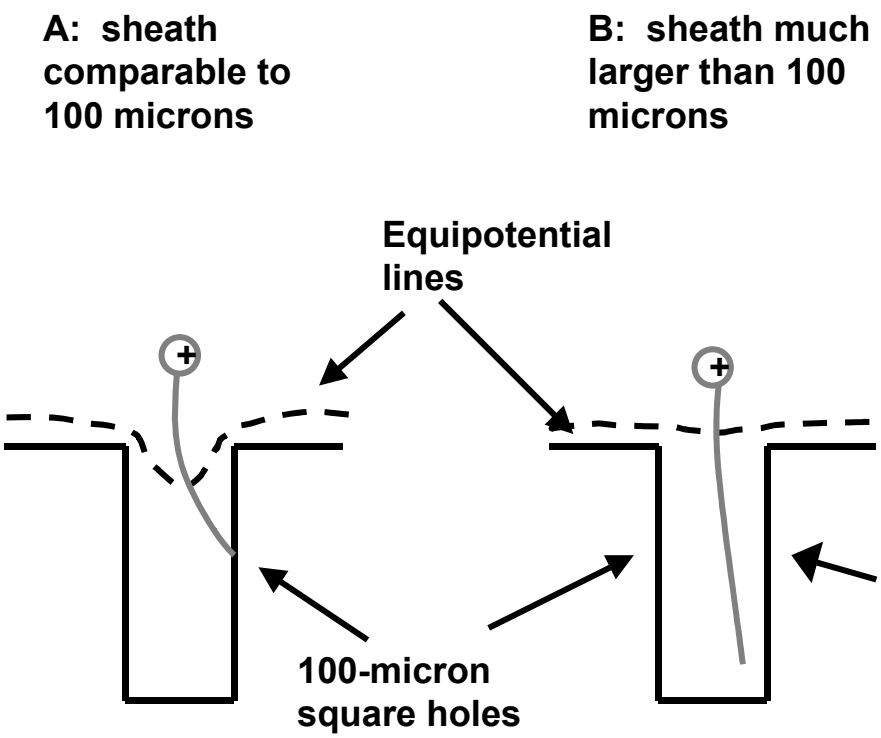

References

[1] E. Kawamura, V. Vahedi, M. A. Lieberman and C. K. Birdsall, Plasma Sources Sci. Technol. **8**(1999) R45-R64

[2] M. A. Sobolewski, Phys. Rev. E **62**(p8540) 2000

[3] D. Bose, T. R. Govindan, and M. Meyyappan, JAP **87**,(10) May 2000, p. 7176

[4] E. A. Edelberg and E. S. Aydil, JAP, **86**(9) Nov. 1999, p.4799

[5] P. A. Miller and M. E. Riley, JAP **82**(8)Oct. 1997 p.3689

[6] J. Hoekstra, M. Grapperhaus, and M. J. Kushner, J. Vac. Sci. Technol A **15** 1913 (1997)

[7] E. Meeks, P. Ho, A. Tingand, R. Buss, J. Vac. Sci. Technol A **16** 2227 (1998)

[8] J. Johannes, T. Bartel, G. Hebner, J. Woodworth, and D. Economou, J. Electrochem. Soc. **144** (7) p.2448 July 1997

[9] A. N. Goyette, Y. Wang, M. Misakian, and J. K. Olthoff, J. Vac. Sci Technol. **A 18**(6) 2785 (2000)

[10] C. A. Nichols, J. R. Woodworth and T. W. Hamilton J. Vac. Sci. Technol. **A 16**(6) 3389 (1998)

[11] U. Kortshagen and M. Zethoff, Plasma Sources Sci, Technol. **4**, 541, (1995)

[12] J. R. Woodworth, M. E. Riley, P. A. Miller, C. A. Nichols, T. W. Hamilton, J. Vac. Sci. Technol. **A 15**(6) 3015 (1997)

[13] J. Hopwood, Appl. Phys Lett. **62**, 940 (1993)

[14] E. S. Aydil, B. O. M. Quiniou, J. T. C. Lee, J. A. Gregus, R. A. Gottscho, Materials Sci. in Semiconductor processing **1,** p. 75, (1998) Pergammon Press, London

[15] K. Kohler, J. W. Coburn, D. E. Horne, E. Kay, J. H. Keller J. Appl. Phys. **57**(1) p.59-66 (1985)

[16] J. Hopwood, Appl. Phys. Lett. **62** (9) p.940 (1993)

[17] M. G. Blain, J. E. Stevens, J. R. Woodworth, and C. E. Nichols, Proceedings of the 9th Conference on Plasma Dynamics and Lasers, Albuquerque, NM June 1998, Americal Institute of Aeronautics and Astronautics.

[18] J. Janes, J. Vac. Sci. Technol. **A 12** (1), 97 (1994)

[19] A. D. Kupyers and H. J. Hopman, J. Appl. Phys. **67** (3), p1229, (1990)

[20] F. Becker, I. W. Rangelow, R.Kassing, J. Appl. Phys **89** (1) p. 56 (1996)

[21] M. Zeuner, H. Neumann, J. Appl. Phys. **81**(7), p. 2985, (1997)

[22] A. Mannenschijn, E van der Drift, G. C. A. M. Janssen, S. Radelaar, J. Appl. Phys. **69**(1) p. 7996, (1991)

[23] P. K. Loewenhardt, H. Hanawa, D. X. Ma, P. Salzman, K. Chuc, A. Sato, V. Todorov, and G. Z. Yin, Proc, Electrochem. Soc. 96, 234 (1996)

[24] J. Trow, Bulletin of the American Physical Society, **39** (6) p. 1488, (1994)

[25] Y. Hikosaka, H. Hayashi, M Sekine, H Tsuboi, M Endo, N. Mizutani, Jpn. J. Appl Phys, **38**, 4465 (1999)

[26] N. Mizutani and T. Hayashi, J. Vac. Sci. Technol. A **19(4)**, 1298, (2001).

[27] E. A. Edelberg, A. Perry, N. Benjamin, and E. S. Aydil, JVSTA **17**(2) Mar. 1999, p. 506

[28] A. Metze, D. W. Ernie, and H. J. Oskam, JAP **60**(9), Nov. 1986, p. 308

[29] J. R. Woodworth, I. C. Abraham, M. E. Riley, R. A. Miller, T. W. Hamilton, B. P. Aragon, R. J. Shul, C. G. Willison, Submitted to JVSTA.

[30] I. C. Abraham, J. R. Woodworth, M. E. Riley, P. A. Miller, T. W. Hamilton, B. P. Aragon, Submitted to JVSTA

[31] P. J. Hargis et. al. Rev. Sci. Inst. **65** (1994) p. 140

[32] P. A. Miller et. al. Journal of Research of the National Institute of Standards and Technology, **100**(4), July 1995, p. 427

[33] R. J. Shul and S. J Pearton "Handbook of Advanced Plasma Processing Techniques", Springer, Berlin, 2000, ISBN 3-540-66772-5, p. 148

[34] V. A. Godyak, R. B. Piejak B. M. Alexandrovitch, Plasma Sources Sci. Technol. 1, 36-58 (1992)

[35] D. N. Ruzic, Electric Probes for Low Temperature Plasmas, AVS monograph M-13, (American Vacuum Society Press, New York, 1994)

[36] R. J. Shul and S. J. Pearton IBID, p. 162

[37] N. Benjamin, Rev. Sci. Instrum. 53, 1541, (1982)

[38] V. A. Godyak, R. B. Piejak, and B. M. Alexandrovich, J. App. Phys. **85** (2) p.703, 15 January 1999

[39] J. R. Woodworth, B. P. Aragon, T. W. Hamilton, Appl. Phys. Lett **70** (15) p. 1947, (1997)

[40] National Aperture, 26 Keewaydin Drive, Salem, New Hampshire, 03079, (603) 893-7393

[41] J. R. Woodworth, M. E. Riley, D. C. Meister, B. P. Aragon, M. S. Le, H. H. Sawin, J. Appl. Phys **80** 1304 (1996)

[42] Unique Wire Weaving Co. Inc. 762 Ramsey Ave. Hillside N.J. 07205

[43] J. R. Woodworth, M. E. Riley, G. A. Hebner, T. W. Hamilton, J. Appl. Phys. **81** (9) 1997, p. 5950

[44] K & L microwave Inc. 22540 Northwood Dr. Salisbury Md, 21801

[45] J. R. Woodworth, P. A. Miller, R. J. Shul, I. C. Abraham, B. P. Hamilton, C. G.

Willison, D. Economou, D. Kim, " Ions near steps – A theoretical and experimental study of Ion Distributions near surface features on rf-biased wafers in plasma etching discharges." Submitted to JVSTA

DISTRIBUTION:

20	MS 1423	G. A. Hebner, 01118
2	MS 1423	J. R Woodworth, 01645
1	MS 0886	I. C. Abraham, 01812
2	MS 1423	G. N. Hays, 01118
1	MS 9018	Central Technical Files, 8945-1
2	MS 0899	Technical Library, 9616
1	MS 0612	Review & Approval Desk, 9612 [For DOE/OSTI]
1	MS 1380	Technology Transfer